A study of the microbial spatial heterogeneity of Bahamian thrombolites using molecular, biochemical, and stable isotope analyses

Artemis S. Louyakis[1], Jennifer M. Mobberley[1], Brooke E. Vitek[2], Pieter T. Visscher[3], Paul D. Hagan[2], R. Pamela Reid[2], Reinhard Kozdon[4,5], Ian J. Orland[5], John W. Valley[5], Noah J. Planavsky[6], Giorgio Casaburi[1], and Jamie S. Foster[1]*

Running Title: Spatial organization of unlaminated thrombolites

[1]Department of Microbiology and Cell Science, University of Florida, Space Life Sciences Lab, Merritt Island, Florida

[2]Rosenstiel School of Marine and Atmospheric Science, University of Miami, Miami, Florida

[3]Department of Marine Sciences, University of Connecticut, Groton, Connecticut

[4]Lamont-Doherty Earth Observatory, Columbia University, Palisades, New York

[5]Department of Geoscience, University of Wisconsin, Madison, Wisconsin

[6]Department of Geology and Geophysics, Yale University, New Haven, Connecticut

*Corresponding Author:

Tel: 321-525-1047; Email: jfoster@ufl.edu

Abstract

Thrombolites are build-ups of carbonate that exhibit a clotted internal structure formed through the interactions of microbial mats and their environment. Despite recent advances, we are only beginning to understand the microbial and molecular processes associated with their formation. In this study, a spatial profile of the microbial and metabolic diversity of thrombolite-forming mats of Highborne Cay, The Bahamas, was generated by using 16S rRNA gene sequencing and predictive metagenomic analyses. These molecular-based approaches were complemented with microelectrode profiling and *in situ* stable isotope analysis to examine the dominant taxa and metabolic activities within the thrombolite-forming communities. Analyses revealed three distinctive zones within the thrombolite-forming mats that exhibited stratified populations of bacteria and archaea. Predictive metagenomics also revealed vertical profiles of metabolic capabilities, such as photosynthesis and carboxylic and fatty acid synthesis within the mats that had not been previously observed. The carbonate precipitates within the thrombolite-forming mats exhibited isotopic geochemical signatures suggesting that the precipitation within the Bahamian thrombolites is photosynthetically induced. Together, this study provides the first look at the spatial organization of the microbial populations within Bahamian thrombolites and enables the distribution of microbes to be correlated with their activities within modern thrombolite systems.

Key words: thrombolites, microbial diversity, metagenome, stable isotopes, microbialites

1. Introduction

With their long evolutionary history, microbialites serve as important model systems to explore and understand the co-evolutionary dynamics among lithifying microbial communities and their local environment. These carbonate structures are formed via the metabolic activity of microbes, which influence and drive biological processes associated with sediment capture and microbiologically induced organomineralization. Microbialites have been found in a wide range of habitats including brackish (e.g., Laval *et al.,* 2000; Breitbart *et al.,* 2009; White *et al.,* 2015; Chagas *et al*., 2016), marine (e.g., Dravis, 1983; Reid *et al.,* 2000; Stolz *et al.,* 2009; Casaburi *et al.,* 2016), and hypersaline (e.g., Logan 1961; Glunk *et al.,* 2011; Wong *et al.,* 2015; Ruvindy *et al.*, 2016; Suosaari *et al.,* 2016; Paul *et al.,* 2016) environments and are classified based on their internal microfabrics (Burne and Moore, 1987; Dupraz *et al.*, 2009). Two of the most well-studied types of microbialites are stromatolites, which exhibit laminated internal fabrics (Walter *et al*., 1994; Reid *et al.,* 2000), and thrombolites with irregular clotted fabrics (Aitken, 1967; Kennard and James, 1986).

Much of our understanding of microbialite formation comes from the study of modern systems (e.g., Reid *et al.*, 2000; Breitbart *et al*., 2009; Petrash *et al*., 2012; Russell *et al*., 2014; Valdespino-Castillo *et al*., 2014; Saghaï *et al.*, 2015; Casaburi *et al.*, 2016; White *et al.*, 2015; Ruvindy *et al*., 2016; Warden *et al.*, 2016; White *et al.*, 2016; Chagas *et al.*, 2016). Microbialites in The Bahamas have been particularly important in expanding research in this area, as they are the only known modern open marine microbialite system and serve as potential analogs to ancient systems (Reid *et al*., 2000). In Bahamian stromatolites, processes underlying formation include iterative growth by cycling microbial mat communities and seasonal environmental controls; the resulting lamination represents a chronology of past surface communities (Visscher *et al.,* 1998; Reid *et al.,* 2000; Bowlin *et al.,* 2012). In thrombolites, the processes that form the clotted fabrics are not well defined. In some

Bahamian thrombolites, the clots appear to be products of calcified cyanobacterial filaments, which through their metabolism cause shifts in the carbonate saturation state and thereby drive precipitation (Dupraz *et al.,* 2009; Planavsky *et al.,* 2009; Myshrall *et al.*, 2010). Alternatively, it has been suggested that the clotted textures in thrombolites are sometimes linked to disruption or modification of microbial fabrics (Planavsky and Ginsburg, 2009; Bernhard *et al*., 2013; Edgcomb *et al*., 2013).

To further explore the formation of clotted fabrics, the thrombolites of Highborne Cay, The Bahamas, were targeted as they represent one of the few modern locations of actively accreting thrombolitic microbialites in open marine environments (Planavsky *et al.,* 2009; Myshrall *et al.,* 2010; Mobberley *et al.,* 2012; Mobberley *et al.,* 2013; Mobberley *et al.,* 2015). These marine thrombolites form in the intertidal zone of a 2.5 km fringing reef complex that extends along the eastern margin of Highborne Cay (Fig. 1A; Reid *et al.,* 1999). The thrombolites range in size from up to one meter in height to several meters in length (Andres and Reid, 2006; Myshrall *et al.,* 2010) and are covered with several distinct microbial mat types (Mobberley *et al.,* 2012).

The dominant mat type associated with the Bahamian thrombolites, referred to as "button" mat, harbors tufts of vertically orientated calcified cyanobacterial filaments (Fig. 1B; Myshrall *et al.,* 2010; Mobberley *et al.,* 2012). The dominant cyanobacterium identified within these tufts with both morphological and molecular tools is *Dichothrix* sp. (Planavsky *et al.,* 2009; Mobberley *et al.,* 2012). At the surface, these *Dichothrix*-enriched button mats are calcified with aragonite precipitates located in the exopolymeric sheath of the cell. With depth, precipitates undergo dissolution and filaments degrade (Planavsky *et al*., 2009). In addition to the tufts of calcified filaments, the thrombolite-forming button mats also harbor a genetically diverse and active microbial community that appears to form vertical gradients of metabolic activity (Myshrall *et al.,* 2010; Mobberley *et al.,* 2013; Mobberley *et al.,* 2015).

Previous work in other microbialite systems, such as stromatolites, has shown that the relationship among active, distinct microbial guilds can alter the local physiochemical environment and generate discrete gradients of both solutes and redox conditions (e.g., Dupraz *et al.,* 2009; Glunk *et al.,* 2011; Wong *et al.,* 2015). Within these microenvironments, the microbial activity can alter both the carbonate saturation index (i.e., carbonate alkalinity and availability of free calcium) and the cycling of exopolymeric substances (EPS; Braissant *et al.,* 2009), which serve as important nucleation sites for precipitation (Dupraz and Visscher, 2005). Certain metabolisms, such as photosynthesis and some types of sulfate reduction, can lead to an increase in pH and thereby promote precipitation (Visscher *et al.,* 1998; Dupraz *et al.,* 2009; Gallagher *et al.,* 2012). Contrastingly, some metabolisms, such as sulfide oxidation, aerobic respiration, and fermentation, can increase dissolved inorganic carbon (DIC) concentrations but lower the pH and carbonate saturation state of the local environment and promote dissolution (Walter *et al.,* 1994; Visscher *et al.*, 1998; Dupraz *et al.,* 2009). Together, it is the parity between categories of metabolisms that determines the extent and net precipitation potential within the lithifying mat community (Visscher and Stolz, 2005).

In addition to the precipitation potential, another component that is critical to the formation of microbialites is the availability of nucleation sites, which can be controlled by the production and degradation of EPS material. The EPS matrix serves several essential roles in the formation of microbialites as it binds cations (e.g., Ca^{2+}) critical for carbonate precipitation, serves as attachment sites for microbes to withstand the high energy wave impacts, and protects microbes from environmental stresses, such as UV exposure and desiccation (Dupraz *et al.,* 2009). Metagenomic analyses of both stromatolites and thrombolites across the globe have shown that Cyanobacteria and Proteobacteria are the two primary producers of EPS material (Khodadad and Foster, 2012; Mobberley *et al.,* 2013;

Mobberley *et al.,* 2015; Casaburi *et al.,* 2016; Ruvindy *et al.,* 2016; Warden *et al.,* 2016). Alteration or restructuring of the EPS through microbial degradation can reduce the cation-binding capability and thereby facilitate the precipitation of calcium carbonate on the EPS matrix (Dupraz *et al.*, 2004; Dupraz and Visscher 2005; Dupraz *et al.,* 2009).

There have been major advances in understanding the processes controlling stromatolite formation; in contrast, the factors controlling carbonate precipitation in thrombolites are less understood. Several recent studies have begun to use meta-omic approaches to understand thrombolite communities and how they may initiate precipitation. For example, metatranscriptomic sequencing of the Bahamian thrombolite-forming mats at midday revealed distinct profiles of gene expression within the thrombolites (Mobberley et al., 2015). This study, however, captured only those metabolically active communities and did not provide a comprehensive assessment of the total microbial population within the observed thrombolites zones. Additionally, previous shotgun metagenomic studies have been used to examine the overall metabolic potential in thrombolite ecosystems, including those at Highborne Cay (Mobberley et al., 2013) and in hypersaline thrombolites of Lake Clifton (Warden et al., 2016); however, neither of these metagenomic studies provided spatial information of the thrombolite-forming communities.

In the present study, we build on this previous research by examining the spatial distribution of the bacterial and archaeal diversity associated with the button mats of Bahamian thrombolites using a targeted phylogenetic marker gene approach coupled with a predictive computational reconstruction of the metagenome to ascertain how thrombolite-forming communities change, both taxonomically and functionally, with depth. These molecular-based approaches are complemented by stable isotope analysis with Secondary Ion Mass Spectrometry (SIMS), a high resolution technique that has not been previously used in any microbialite study, to provide additional constraints on carbonate precipitation in the

Dichothrix calcified filaments. Together, these methodologies elucidate the juxtapositioning of the taxa and metabolic functions associated with the thrombolite-forming mats as well as provide key insight into the metabolic metabolisms that initiate precipitation within these lithifying ecosystems.

2. Methods

2.1. Sample collection

Thrombolite-forming button mats were collected from the island of Highborne Cay, The Bahamas, (76°49' W, 24°43'N) in February 2010 and October 2013 from an intertidal thrombolitic platform from Site 5 (Andres and Reid, 2006). The 2010 mats were partitioned in the field into three distinct vertical sections (0 – 3 mm; 3 – 5 mm; and 5 – 9 mm depth horizons, respectively) with a sterile scalpel to cut the thrombolite-forming mats, and the sections were immediately placed into RNAlater (Life Technologies, Inc., Grand Island, NY). These samples were transported to Space Life Sciences Lab, Merritt Island, Florida, where they were stored at -80°C until processing. The 2013 mats were processed for isotope analyses as described below.

2.2. Microelectrode measurements

Depth profiles of oxygen, sulfide, and pH were determined in triplicate with needle microelectrodes (Visscher *et al.,* 1991, 1998; Pages *et al.,* 2014) either *in situ* or *ex situ* under ambient temperature and light intensity. Microelectrodes with a tip diameter between 60 and 150 µm were deployed in 250 µm depth increments with a manual micromanipulator (National Aperture, Salem, NH). Oxygen profiles were measured in submerged mats (in ca. 5-15 cm water) with a polarographic Clark-type needle electrode with an outer diameter of 0.4 mm, and readings were recorded with a picoammeter (PA2000; Unisense, Aarhus,

Denmark). Polarographic sulfide electrodes (Unisense, Denmark) were used in combination with a Unisense PA 2000 picoammeter, and pH and S^{2-} electrodes (Diamond General, Ann Arbor, MI) were connected to a high-impedance millivolt meter (Microscale Measurements, The Netherlands). Both electrode types were encased in needles (outer diameter 0.5 mm). Sulfide electrodes were calibrated before and after each deployment with buffers of three different pH values that span the pH range observed in the thrombolite (i.e., pH 7, 8, and 9). Under an oxygen-free atmosphere, aliquots of a sulfide stock solution were added in increments to the buffer, and electrode signals were recorded. Subsamples of the buffer were taken to ascertain the actual concentration of sulfide in the calibration cocktail by using the methylene blue method. The pH electrodes were calibrated at pH 5, 7, and 10. The pH profiles were used to calculate the actual sulfide concentration at each depth.

2.3. Generation and sequencing of 16S rRNA gene libraries

DNA was extracted in triplicate from each vertical section with a modified MoBio PowerSoil DNA isolation kit that included a xanthogenate pre-treatment, as previously described (Green *et al*., 2008). The DNA was then PCR amplified in triplicate with fusion 454-primers that included a unique eight base pair barcode on the 3' end (Supplemental Table S1). The PCR reactions for the bacterial 16S rRNA libraries targeted the V1-2 region and included the following: 1 x Pfu Reaction Buffer (Stratagene, La Jolla, CA), 280 µM dNTPs, 2.5 µg bovine serum albumin (BSA), 600 nM of each primer, 1 ng of genomic mat DNA, 1.25 U of Pfu DNA Polymerase (Stratagene, La Jolla, CA), and nuclease-free water (Sigma, St. Louis, MO) in a volume of 25 µl. The amplification parameters included a 95°C denaturation for 5 min, followed by 30 cycles of 95°C for 1 min, 64°C for 1 min, 75°C for 1 min, and a final extension at 75°C for 7 min.

The archaeal libraries required a nested PCR approach that included two rounds of amplification and targeted the V3-5 region. The reactions contained the same concentrations as the bacterial library with the exception of 400 nM of 23F and 958R primers (Delong, 1992; Barns *et al*., 1994) and 10 ng of thrombolitic mat DNA in round one, whereas 400 nM of primers 334F and 915R (Casamayor *et al*., 2002) with 10 ng of round one amplicon material as a template. The amplification parameters in round one included a denaturation step of 95°C for 2 min, followed by 35 cycles of 95°C for 30 sec, 55°C for 1 min, 72°C for 2 min with an extension of 72°C for 10 min. In round two the parameters were similar except that the annealing temperature was changed to 61°C.

For each library, the PCR amplicons were purified with the Ultraclean PCR Clean-Up Kit (MoBio, Carlsbad, CA) and combined into equimolar ratios. Sequencing was performed per manufacturers protocol by a 454 GS-FLX platform with Titanium chemistry (Roche, Branford, CT) at the University of Florida's Interdisciplinary Center for Biotechnology Research. The raw sequence data files were deposited into the NCBI sequencing read archive under number SRP068710 (bacteria) and SRP068710 (archaea) under project PRJNA305634.

2.4. Bioinformatic analysis of 16S rRNA gene libraries

The recovered bacterial and archaeal 16S rRNA gene sequences were analyzed by Quantitative Insights Into Microbial Ecology (QIIME; version 1.9.1; Caporaso *et al*., 2010). Preprocessing was completed to separate the replicate libraries by depth, remove barcode adaptors, and filter for quality by using default parameters including: minimum sequence length of 200 bp; maximum sequence length of 1000 bp; minimum quality score of 25; maximum ambiguous bases of 6; and maximum homopolymer length of 6. Operational taxonomic units (OTUs) were assigned to the filtered reads at 97% identity against the Greengenes database (v13.8; DeSantis *et al*., 2006) using the UCLUST method within

QIIME. Further filtering was completed including removal of unassigned reads and filtering for most abundant OTUs (> 0.005%). The generated OTU table was used for taxonomic comparison, filtering the OTUs at 0.005% and producing taxonomic trees with Meta Genome Analyzer (MEGAN5; Huson *et al.*, 2007). OTU tables were filtered at 0.1%, and hierarchal taxonomic pie charts were created with the Krona tool (Ondov *et al*., 2011). The representative sequences were aligned with PyNAST (v1.2.2; Caporaso *et al*., 2010) to the Greengenes Core reference alignment and a phylogenetic tree was built by FastTree (v2.1.3; Price *et al*., 2010). The phylogenetic tree was used for downstream community analyses. Diversity analyses were performed at a sequence depth of 3587 for archaea and 3691 for bacteria.

Alpha diversity indices were calculated by using observed species and Faith's Phylogenetic Diversity (PD) measure (Faith, 1992), and the averaged results were used to generate rarefaction curves. Beta diversity comparisons were visualized by using Principal Coordinates Analyses (PCoA) and Emperor (Vázquez-Baeza *et al*., 2013) generated from unweighted UniFrac distance matrices (Lozupone and Knight, 2005). Statistical significance between the mat depths was calculated by adonis, a nonparametric, permutation-based metric.

2.5. Reconstruction of functional metagenome using the PICRUSt algorithm

Functional gene content from each of the three vertical sections was predicted from the recovered 16S rRNA gene sequences by using the algorithm Phylogenetic Investigation of Communities by Reconstruction of Unobserved States (PICRUSt v.1 .0; Langille *et al*., 2013), as previously described (Casaburi *et al.,* 2016). Results were collapsed at Kyoto Encyclopedia of Genes and Genomes (KEGG) Orthologs (KO) Level 3 within the pathway hierarchy of KEGG (Kanehisa and Goto, 2000). For comparison purposes, a shotgun

metagenomic dataset of whole Bahamian thrombolite-associated mats previously collected from Highborne Cay (Mobberley *et al.,* 2013**)** was downloaded from the MG-RAST database with accession number 4513715.3. Raw reads were filtered by SICKLE (v. 1.2; Joshi and Fass, 2011) with default parameters. Filtered reads were re-annotated for functionality at different KEGG levels by the Metagenome Composition Vector (MetaCV v. 2.3.0) with default parameters (Liu *et al*., 2012). Resulting hits were filtered at a correlation score > 30, collapsed at KO Level 3, and finally compared to the 16S rRNA gene predicted functional profile.

2.6. Bulk stable isotope analysis

Samples of thrombolite-forming mats were collected for isotopic analysis during the same collection trip as the molecular samples from Site 5 (Andres and Reid, 2006) of Highborne Cay in October 2013. The mat samples were dried and examined by bulk isotope analysis for both inorganic and organic signatures. Calcified filaments were dissected from the button mats, dried, and ground to a fine powder in triplicate. Aliquots of the carbonate (i.e., aragonite; Planavsky et al., 2009) were measured for inorganic $\delta^{13}C$ and $\delta^{18}O$ with a Finnigan-MAT 252 isotope ratio mass spectrometer coupled with a Kiel III carbonate preparation device.

For isotopic analysis of organic matter, calcified filaments were dissected and treated with an acid solution (6N HCl) at room temperature overnight until all $CaCO_3$ was removed and rinsed with distilled water to remove HCl. Samples were loaded into tin capsules and placed in a 50-position automated Zero Blank sample carousel on a Carlo Erba NA1500 CNHS elemental analyzer. After flash combustion in a quartz column containing chromium oxide and silvered cobaltous/cobaltic oxide at 1000°C in an oxygen-rich atmosphere, the sample gas was transported in a He carrier stream and passed through a hot reduction column

(650°C) consisting of reduced elemental copper to remove oxygen. The effluent stream then passed through a chemical (magnesium perchlorate) trap to remove water followed by a 3 meter GC column at 45°C to separate N_2 from CO_2. The sample gas next passed into a ConFlo II preparation system and into the inlet of a Thermo Electron Delta V Advantage isotope ratio mass spectrometer running in continuous flow mode where the sample gas was measured relative to laboratory reference N_2 and CO_2 gases. All carbon and oxygen isotopic results are expressed in standard delta notation relative to Vienna Pee Dee Belemnite (VPDB), whereas nitrogen isotopic results are expressed in standard delta notation relative to air (AIR). The standard used for bulk C and O measurements was NBS-19, whereas USGS40 and USGS41 were used for N. Measurements were conducted in triplicate at the Light Stable Isotope Mass Spectrometry Laboratory in the Department of Geological Sciences at the University of Florida. Instrument precision was better than 0.10‰ for all bulk isotope measurements.

2.7. Stable isotope analysis using Secondary Ion Mass Spectrometry (SIMS)

Additional mat samples, collected in Oct 2013, were prepared as thin-sections at the WiscSIMS laboratory, UW-Madison. Samples were cast with EpoxiCure resin in 25 mm epoxy rounds, cut with a Buehler IsoMet™ low speed to expose the most suitable section for analysis, and turned, together with two grains of UWC-3 WiscSIMS calcite standard ($\delta^{13}C$ = -0.91 ±0.04‰; $\delta^{18}O$ = -17.87‰ ± 0.03‰ VPDB (Kozdon *et al.*, 2009), into ~100 µm-thick thin sections. An aragonite standard (UWArg-7, $\delta^{13}C$ = 5.99‰; $\delta^{18}O$ = -10.84‰ VPDB; Orland, 2012; Linzmeier et al., 2016) was also run at the beginning of each day of analysis to correct for the differences in instrumental mass fractionation between calcite and aragonite, which was 1.3‰ for $\delta^{18}O$ and 1.5‰ for $\delta^{13}C$. The epoxy rounds were ground to expose features of interest for analysis. Petrographic microscopy was conducted with an Olympus

BH-2 microscope with plane-polarized and cross-polarized transmitted light at various magnifications to identify potential sites suitable for SIMS analysis. The samples were then polished and sputter coated with palladium for scanning electron microscopy (SEM) at the University of Miami's Center for Advanced Microscopy (UMCAM) to identify areas of precipitate for analysis and to screen for potential textural anomalies that might impede *in situ* $\delta^{13}C$ and $\delta^{18}O$ measurements. The SEM analysis was conducted on a FEI XL-30 Field Emission ESEM/SEM instrument with energy dispersive spectrometer (EDS). The SEM analysis was to insure integrity of the sample and to identify specific target sites. After SEM analysis, the palladium coating was removed with 0.25 μm polish on a lapidary wheel, dried, and recoated with gold.

The thrombolite mat samples were then analyzed for $\delta^{13}C$ and $\delta^{18}O$ on a CAMECA ims-1280 secondary ion microprobe mass spectrometer (SIMS) using a $^{133}Cs^{+}$ primary ion beam at the WiscSIMS Laboratory, Department of Geoscience, University of Wisconsin-Madison. A primary beam of 600 pA, with mean 0.77 ‰ spot-to-spot precision (2SD), was used for $\delta^{13}C$, and 1.7 nA was used for $\delta^{18}O$ with a 10 μm spot size (precision ~0.3‰). WiscSIMS carbonate analysis has been described in detail in previous publications (Orland *et al*., 2009; Valley and Kita, 2009; Kozdon *et al*., 2011; Williford *et al.,* 2016).

Analysis of the thrombolitic mat sections (10 – 15 spot analyses per sample) were bracketed by 8 - 10 repeat measurements on the UWC-3 standard grain by using the same parameters as the samples to help determine instrumental mass fractionation corrections for each set of measurements. After completion of each analytical session, the samples were returned to University of Miami for SEM inspection of the pits to evaluate any features that may have impacted accuracy (e.g., cracks or epoxy). Additionally, for those measurements that penetrated down to epoxy material (depths of 1-2 μm) and had high secondary ion count rates (i.e., > 100% for ^{12}C of the measured counts per second on the standard grain), the final

three to six cycles (of 20) were excluded from computations, and the values for the spots were recalculated as in the work of Vetter *et al*. (2014). Visualization of the data was conducted in R (v.3.2.2; R Core Team, 2015) by using the package ggplot2 (Wickham, 2009).

3. Results

3.1. Microelectrode profiling of thrombolite button mats

The *in situ* concentrations of oxygen and sulfide were measured with microelectrodes during early afternoon representing peak photosynthesis (i.e., 12:30pm and 2:00pm) and at the end of the night, which marks the end of a prolonged anoxic period (i.e., 4:00am – 6:00am) (Fig. 1C). The profiles reveal steep vertical gradients that fluctuated throughout the diel cycle. During the day, the oxic zone extended through the first 5 mm of the button mat with the peak of oxygen production (> 600 μM) occurring in the upper 3 mm (Fig. 1C). At night, however, oxygen levels decreased significantly and were detectable only in the upper 2 mm of the mat suggesting rapid consumption at night and limited diffusion of O_2 from the overlying water column. Contrastingly, sulfide levels were low during the day with levels detectable only below 6 mm. At night, sulfide levels built-up and were detectable at 4 mm with a peak concentration occurring at a depth of 8 - 10 mm within the mat.

In addition to oxygen and sulfide, pH was also monitored throughout the vertical profile of the button mat revealing a wide shift throughout the diel cycle. At peak photosynthesis, the localized pH ranged from 8.4 to 10.4 throughout the depth profile with the highest pH occurring at a depth of 3 mm (Fig. 1C). At night, however, the pH steadily decreased to as low as 7.1 at depths below 5 mm. Based on these oxygen, sulfide, and pH microelectrode profiles three distinct spatial zones emerged. Zone 1 included the upper 3 mm of the button mat and contained a supersaturated oxic zone that was suggestive of high

rates of oxygen production and consumption. Zone 2 represented a transitional area 3 – 5 mm beneath the surface where oxygen levels decreased and sulfide levels began to build. Finally Zone 3, which included depths below 5 mm, represented a primarily anoxic region of the thrombolite-forming mat.

3.2. Phylogenetic composition of Bacteria in thrombolite communities with depth

Immediately after the microelectrode profiles were generated, the thrombolite mats were then sectioned based on these three observed zones (Zone 1, 0 – 3 mm; Zone 2, 3 – 5mm; and Zone 3, 5 – 9 mm), and each of these spatial regions was subsequently examined for taxonomic diversity (Fig. 1D). Three replicate amplicon libraries were generated for each zone targeting the 16S rRNA gene for both the Bacteria and Archaea. A summary of the data associated with the amplicon libraries is provided in Table 1. The overall bacterial diversity increased with depth (Supplemental Fig. S1A) with 2044 operational taxonomic units (OTUs) at 97% sequencing similarity in the upper oxic Zone 1 and 2947 and 3525 OTUs recovered from Zone 2 and 3, respectively. The number of recovered OTUs was much higher then previous diversity assessments of the Highborne Cay thrombolites (Myshrall *et al.,* 2010; Mobberley *et al.,* 2012) and likely reflects the increased sequencing coverage as determined by Good's estimates (Table 1).

A total of 16 phyla were recovered from the three spatial zones within the thrombolite-forming mat with the Proteobacteria, Cyanobacteria, Bacteroidetes, Chloroflexi, and Acidobacteria being highly represented in each zone (Supplemental Fig. S2). Distinct taxonomic differences, however, were observed across the three spatial regions of the thrombolite mat at the family level (Fig. 2, 3; Supplemental Fig. S2). In the upper Zone 1, the most abundant family represented within the mat is the cyanobacterial family Rivulariaceae (Fig. 2; Supplemental Fig. S2). This taxon contains the genus *Dichothrix*, which was

previously identified in the thrombolite mats as forming extensive tufts of calcified filaments (Fig. 1B) and has rarely been found in laminated stromatolites (Foster and Green, 2011). The Rivulariaceae dominated the oxic Zone 1 comprising 21% of annotated reads compared to 15% in the transitional Zone 2 and only 5% of the total recovered reads in Zone 3 (Fig. 2; Supplementary Fig. S2). In addition to Rivulariaceae, other prevalent Cyanobacteria in the oxic Zone 1 included Pseudanabaenaceae (11%), Xenococcaceae (5%), and Synechococcaceae (4%; Fig. 2; Supplemental Fig. S2).

Although Cyanobacteria was the dominant phylum recovered from Zone 1, there was also a diverse population of Proteobacteria, specifically, the class Alphaproteobacteria. Within the Alphaproteobacteria there was enrichment of the photoheterotrophic Rhodobacteraceae (19%) and Rhodospirillaceae (7%) families, and to a lesser extent the Rhizobiales (5%). These taxa were not only abundant in Zone 1 but were highly represented throughout the thrombolite vertical profile (Fig. 3; Supplemental Fig. S2). Other proteobacterial taxa that were abundant in Zone 1 compared to the other two zones included the sulfate-reducing Deltaproteobacteria family Desulfovibrionaceae (3%) and the Gammaproteobacteria family Thiotrichaceae (0.8%), which harbors several sulfide-oxidizing taxa (Fig. 3). A detailed krona plot of the upper 3 mm of the thrombolite mat is provided in Supplemental Fig. S3.

Zone 2 represented a transitional phase in the thrombolite-forming mats with several taxa first appearing in this 3 – 5 mm zone and gradually increasing in relative abundance in the anoxic Zone 3 (Fig. 3; Supplemental Fig. S2, S4). For example, in the Deltaproteobacteria the sulfate-reducing families Desulfobacteraceae and Syntrophobacteraceae were enriched in Zones 2 and 3 compared to Zone 1. Additionally, the purple sulfur bacterial Gammaproteobacteria family Ectothiorhodospiraceae (order Chromatiales) and the sulfide-oxidizing Piscirickettsiaceae (order Thiotrichales) also

exhibited a gradual increase in relative abundance with depth (Fig. 3). In addition to the more prevalent taxa there were several families that appeared to a lesser extent only at depth and included the photoheterotrophic Gemmatimonadetes, purple non-sulfur bacteria Rhodobiaceae, and nitrite-oxidizing Nitrospiraceae. Detailed taxonomic profiles of Zone 2 and 3 are depicted as krona plots in Supplementary Figs. S4 and S5.

In addition to analysis of the bacterial composition, a beta diversity analysis was completed to assess whether these observed taxonomic differences were statistically significant. Unweighted UniFrac distance matrices were generated for the Bacteria amplicon libraries and visualized with a jackknifed principal coordinate analysis (PCoA; Fig. 4A). The statistical analyses revealed that each of the three spatial zones represented distinctive bacterial communities with low standard deviation amongst the library replicates (Fig. 4A). The R^2 value showed an effect size of 0.402, indicating that approximately 40% of the variation in the bacterial populations could be explained by depth and potentially other environmental factors within the mats ($p=0.001$; $R^2=0.402$, adonis; Fig. 4A). Depth likely accounted for at least 27% (PC1) of the variation among the three zones based on the PCoA plots (Fig. 4A).

3.3. Phylogenetic composition of Archaea in thrombolite communities with depth

With regard to the overall archaeal diversity (e.g., Shannon Index), there was little difference across the three zones with the recovered OTUs ranging from 506 to 671 (Table 1; Supplementary Fig. S1B). Of the three recovered phyla, the Thaumarchaeota were dominant in all three zones of the thrombolite forming mats with most of the reads sharing similarity to the ammonia-oxidizing family Cenarchaeaceae (Fig. 5), specifically the genus *Nitrosopumilus*. There were, however, some taxonomic differences between the different spatial regions in the thrombolites. For example, phototrophic Halobacteriales showed the

highest abundance in the upper oxic Zone 1, as did the ammonia-oxidizer Nitrososphaeraceae (Fig. 5). Although few methanogenic archaeal taxa were detected in each of the three zones, they had the highest representation in the transitional Zone 2 with most of the reads sharing similarity to the class Thermoplasmata and the family Methanocarcinaceae (Fig. 5). A beta diversity test was also completed for the archaeal libraries and showed increased statistical variation between replicates (Fig. 4B). Although the archaeal populations did not have as high of an effect size (R^2) as the bacterial population, 30% of variation within the archaea could be explained by environmental factors, such as depth. Based on the beta diversity analysis, just as in the bacterial population, the three zones did appear to have spatially distinct Archaea populations with approximately 20% of the variation between the zones likely being associated with depth ($p=0.017$; $R^2=0.307$, adonis; Fig. 4B).

3.4. Spatial profiling of functional gene complexity of thrombolite-forming mats using predictive sequencing analysis

In addition to profiling the microbial diversity within the thrombolite button mat, a reconstruction of the functional gene complexity was generated for each zone by using the 16S rRNA gene sequences and the PICRUSt algorithm (Langille *et al.,* 2013). As the number of available reference genomes has steadily increased, PICRUSt has emerged as an effective tool to accurately predict the functional complexity of the metagenomes based on taxonomic information (Langille *et al.,* 2013). The tool has successfully been used to reconstruct the metagenomes of a wide range of ecosystems including nonlithifying microbial mats and stromatolites (Langille *et al.,* 2013; Casaburi *et al.,* 2016). A predicted metagenome was generated for each spatial zone with the QIIME taxonomic output, which was then statistically compared to a previously published metagenome of the entire button mat (0 – 9 mm; Mobberley *et al.,* 2013) to determine whether differences in the metabolic capabilities

could be observed between zones. The previously sequenced thrombolite metagenome was re-annotated by using MetaCV to update the metagenomic dataset and enabling comparable annotations to the PICRUSt predictive metagenomes.

A total of 272 KEGG functions were identified in the three zones corresponding to 328 level 3 KO entries, which was consistent with the 268 KEGG functions observed in the re-annotated whole-mat metagenome (Supplemental Table S2). Additionally, there was a strong correlation between the PICRUSt predictive metagenomes and the whole mat metagenome ($r = 0.93$, Pearson), with most of the KOs ($n = 222$) showing little or no variation between zones (Supplemental Table S2). Of the 59 KOs that did show variation (> 0.1%), several of the differences occurred between the upper oxic Zone 1 and the two deeper Zones 2 and 3 (Fig. 6). In Zone 1, there was an increase in the relative abundance of KO pathways associated with photosynthesis including the antennae proteins, porphyrin, and chlorophyll metabolism, whereas there was a lower abundance of genes associated with carboxylic acid metabolism (e.g., butanoate, benzoate, caprolactam metabolism; Fig. 6). Deeper within the mat in Zones 2 and 3 there was a higher relative abundance of genes associated with fatty acid metabolism and lipopolysaccharide (LPS) biosynthesis compared to Zone 1. Despite these few select differences, many highly represented pathways in the thrombolite-forming mats, such as DNA repair proteins, two-component signaling, and bacterial motility, showed no differences among the three spatial zones and likely reflect the central metabolisms associated with the thrombolite microbiome.

3.5. Stable isotope analyses of thrombolitic carbonates

The calcified carbonate filaments associated with the *Dichothrix* cyanobacteria in the upper Zone 1 were examined by using a combined bulk isotopic analysis and targeted SIMS approach coupled, which enabled an *in situ* high-spatial resolution analysis (Valley and Kita

2009; Kozdon *et al.,* 2009; Kita *et al.,* 2011) (Fig. 7). Bulk samples of dissected calcified filaments had $\delta^{18}O$ values with a mean of -0.5 ± 0.1‰ VPDB suggesting that the precipitates associated with the filaments were not the result of evaporation, which would cause an enrichment in heavy isotopes. Bulk $\delta^{13}C_{carb}$ values of the dissected filaments had a mean of 5.0 ± 0.03‰, which was similar to the surrounding carbonate sediments within the thrombolite structure (+4.0‰ to +4.9‰; mean = 4.6 ± 0.3‰). The $\delta^{13}C$ values for the organic matter associated with the filaments was depleted compared to the sediment with values ranging -9.9‰ and -9.2‰ (mean = -9.6 ± 0.2‰), suggesting a relatively muted fractionation during organic matter uptake, similar to what has been produced in other modern microbial mats (Canfield and DesMarais, 1993). The $\delta^{15}N_{org}$ values associated with the filaments ranged from -1.1‰ to -0.1‰ (mean = -0.8 ± 0.3‰), suggesting that nitrogen fixation is a predominant means of N assimilation (Sigman *et al*., 2009) within the thrombolite-forming mats and correlates with the high number of recovered diazotrophic Cyanobacteria and Alphaproteobacteria from the mats.

To complement the bulk stable isotope analyses, the calcified filaments were also analyzed *in situ* with SIMS to provide a higher spatial resolution (10 μm spot size) of the $\delta^{18}O$ and $\delta^{13}C$ compositions of the calcified filaments. Micrographs depicting the SIMS target sites along the filaments and associated carbonate precipitate are shown in Fig. 8. The $\delta^{18}O$ value of the surrounding carbonate sediments ranged from -2.0‰ to -0.6‰ (mean = -1.3 ± 0.5‰), whereas the filaments exhibited a more depleted oxygen signature ranging from -7.7‰ to -2.0‰ (mean = -3.2 ± 1.1‰) (Fig. 7). The $\delta^{13}C$ values of the surrounding sediments (i.e., ooids) in the thrombolite button mats had a narrow range of values (+3.6‰ to +4.6‰; mean = 4.1 ± 0.4‰) and matched values from previous studies of sediments that surround the thrombolite structures (e.g. ooids; Swart and Eberli, 2005), whereas the filaments had a much

wider range (+0.1‰ to +5.5‰; mean = 2.7 ±1.3‰). All stable isotope measurements are presented in order of analysis in supplementary Tables S4-S5.

4. Discussion

4.1. Microbial diversity within thrombolite-forming mats are highly structured

The presence of discrete spatial zones of microbial and biochemical activity have been well documented in stromatolites (e.g., Visscher *et al.,* 1998; *Wong et al.*, 2015); however, the occurrence of similar zonation in mats that form clotted thrombolites has only been recently suggested (Mobberley *et al.,* 2015). In this study, statistical analysis of the bacterial and archaeal communities revealed significantly different profiles of taxa with depth (Fig. 4) suggesting the microbes are not only active at different depths (Mobberley et al., 2015) but that there are also distinct populations that are forming discrete microenvironments within the thrombolite-forming mats.

In the upper oxic Zone 1, the dominance of cyanobacterial sequences with similarity to the filamentous Rivulariaceae reinforces the morphological observation that *Dichothrix* sp., a member of the Rivulariaceae, serves as a "hot spot" for photosynthetic activity and carbonate deposition within the thick EPS matrix associated with the filaments (Planavsky *et al.,* 2009). Future sequencing of the *Dichothrix* sp. genome will help to expand the relatively small database of filamentous, heterocystous cyanobacteria as well as delineate the specific pathways associated with EPS production in this keystone organism. In addition to the cyanobacteria, taxonomic analyses also revealed an enrichment of diazotrophic photoorganoheterotrophs primarily associated with the Rhodobacterales, Rhodospirillales, and Rhizobiales increasing with depth (Fig. 3). These metabolically flexible Alphaproteobacteria are ubiquitous in marine microbial communities including all previously characterized microbialites, coral symbioses, and sediments (e.g., Dang *et al.,* 2013;

Houghton *et al.,* 2014; Wong *et al.,* 2015; Casaburi *et al.,* 2016; Hester *et al.,* 2016; Suosaari *et al.,* 2016) and may be contributing to the carbon fixation rates deeper within the thrombolitic mats where there are fewer cyanobacteria due to the reduced light levels and the presence of sulfide. Additionally, the diazotrophic photoheterotrophs may be helping to maintain the bioavailability of nitrogen in the thrombolite-forming communities.

Another key microbial functional group enriched within the thrombolite-forming communities was sulfate-reducing bacteria (SRB), whose activity has been directly correlated to deposition of carbonate in actively accreting stromatolites (Visscher *et al.,* 2000; Decho *et al.*, 2010). There was a pronounced vertical stratification of SRB in the thrombolite-forming communities. Taxa associated with Desulfovibrionaceae were enriched in the upper oxic Zone 1, whereas the Desulfobacteraceae increased in their relative abundance with depth. This vertical stratification of SRBs has been seen in the non-lithifying hypersaline mats of Guerrero Negro, Mexico (Risatti *et al.,* 1994) and Solar Lake Egypt (Minz *et al.,* 1999). Several species of sulfate-reducing Desulfovribionaceae (e.g., *Desulfovibrio* spp. and *Desulfomicrobium* spp) have been shown to be prevalent in the oxic zone of microbial mats (Krekeler *et al.,* 1997), and high levels of sulfate reduction activity have been recorded in the upper oxic zone of non-lithifying and stromatolite-forming mats (e.g., Canfield and DesMarais, 1991; Visscher *et al.,* 1992, 2000). The abundance of SRB in the oxic zone may be, in part, due to the presence of sulfide-oxidizing bacteria (SOB). There was an enrichment of the families Thiotrichaceae and Chromatiaceae in the upper Zone 1, which are known to harbor many sulfide-oxidizing taxa (Pfennig and Trüper, 1992; Lenk *et al.*, 2011). The SOB may be removing the O_2 and S^{2-} generated by the cyanobacteria and SRBs, both of which can be toxic to the SRB at high enough levels (Decho *et al.*, 2010). Together, this enrichment of SOB, oxygen-tolerant SRB, and their vertical stratification in the thrombolite-forming may suggest that, much like the stromatolites, these different phylogenetic groups may be playing

distinctive community functions in response to variable carbon and electron donor availability at different depths as well as the diel flux of oxygen and sulfide.

The archaeal population also exhibited stratification of certain taxa within the thrombolite-forming mat. There was an enrichment of Halobacteriales in the upper oxic Zone 1 of the thrombolitic mats. Members of this order are typically chemoorganoheterotrophic and can grow on a wide range sugars, carboxylic acids, alcohols, and amino acids. This aerobic taxon has been observed in both lithifying and nonlithifying microbial mat communities primarily in hypersaline environments (Burns *et al.,* 2004; Arp *et al.,* 2012; Schneider *et al.,* 2013) and may be contributing to the heterotrophic degradation of EPS material associated with the calcified filaments. It should be noted that the salinity of the porewater in the upper part of the microbialites increases significantly (~135 PSU; Visscher unpubl) upon exposure to the atmosphere during low tide, creating temporary hypersaline conditions.

Sequences were also recovered from methanogenic archaea in primarily Zone 2, and these were primarily associated with the Methanocarcinaceae and Thermoplasmata. These taxonomic results correspond to recovered methyltransferase-encoding genes in the thrombolite metagenome (Mobberley *et al.,* 2013), and there was an enrichment of recovered sequences from Zone 2 (Fig. 5). Members of the Methanocarcinaceae can perform methanogenesis using CO_2, acetate, and C_1 compounds (Feist *et al.,* 2006) and have been shown to elevate pH levels in mat communities via CO_2 consumption (Kenward *et al.,* 2009). More recently, methanogenic lineages of the Thermoplasmata have been identified in human and rumen gut microbiomes as well as wastewater sludge habitats that also can use methanogenic substrates (Dridi *et al.,* 2012; Poulson *et al*., 2013; Iino *et al*., 2013). Although not the dominant archaea within the thrombolite-forming mats, the recovered taxa in this study coupled with functional genes observed in the thrombolite metagenome (Mobberley *et*

al., 2013) suggest that methanogenesis may have a potential, albeit minor, role in promoting an alkaline environment within these thrombolitic mats. Methane production has been observed within the thrombolites and adjacent stromatolites (Visscher unpublished), and further work to more fully characterize methane levels within each zone may help elucidate the role of methanogenesis, if any, in the Bahamian thrombolite formation.

By far the largest component of the archaeal population within the thrombolite forming mat were the Thaumarchaeota specifically Cenarchaeaceae, which harbor many ammonia-oxidizing taxa (Fig. 5). Although the Cenarchaeaceae were found in all three zones, there was an enrichment in the lower two regions of the mat (Fig. 5). Thaumarchaeota have been found in a wide range of lithifying and non-lithifying microbial mat habitats (e.g. Ruvindy et al., 2016) and likely play a role in nitrogen cycling within the thrombolite-forming communities. Previous studies in which the metagenomics of lithifying systems have been examined found a paucity of bacterial nitrification genes (Breitbart et al., 2009; Mobberley et al., 2013; Ruvindy et al., 2016), and ammonia-oxidizing archaea, such as those taxa within the Thaumarchaeota, may be facilitating the metabolism of ammonia to nitrite.

4.2. Predictive metagenome reconstruction shows strong correlation with taxa and function.

The PICRUSt predictive metagenome strongly correlated ($r = 0.93$) with the previously published whole shotgun library, which had targeted the entire thrombolite-forming mat community and provided no spatial information regarding the metagenome (Mobberley *et al.,* 2013). The PICRUSt reconstruction identified key differences between the different spatial zones thereby providing further evidence that 16S rRNA gene libraries can provide useful insight into the metabolic capabilities of microbial ecosystems. For example, there was extensive overlap in the relative abundance of functional genes between the different depths in several pathways, such as nucleotide and amino acid metabolism, genetic

information processing, and environmental information responses with the shotgun sequence library suggesting there are key central metabolisms in the thrombolite-forming mat microbiome at all depths (Fig. 6). Additionally, genes associated with several key metabolisms associated with the promotion (e.g., photosynthesis, sulfate reduction) and dissolution (e.g., sulfide oxidation, fermentation, ammonia oxidation) of carbonate precipitation were observed within the thrombolite-forming mats.

Despite the extensive overlap between the core metagenome at each depth, differences were observed between the mat zones. The enrichment of genes associated with photosynthesis pathways in the upper Zone 1 and the increase of genes associated with different carboxylic, fatty acid and LPS metabolisms deeper within the mat reveal distinctive metabolic transitions throughout the mat profile. The increase in LPS production at depth likely reflects the oxygen-limiting environment deeper in the thrombolite-forming mat. Previous studies with model organisms, such as *Escherichia coli* and *Pseudomonas aeruginosa*, have shown that anaerobic conditions can positively regulate production of LPS (Landini *et al*., 2002; Sabra *et al*., 2003). These spatial differences in metabolic capabilities are also reflected in the biochemical gradients observed within the mats (Fig. 1). These functional genes could serve as ideal targets to examine the potential regulation of these metabolisms within the thrombolite ecosystems potentially providing insight into the molecular response to changing environmental variables, such as pH, oxygen, and sulfide. Additionally, by tracking these specific molecular pathways, it may be possible to elucidate the specific genes and taxa involved in the diagenetic alteration of organic material in the thrombolites over both spatial and temporal scales, which represents an important area of future microbialite research.

4.3. Stable isotope profiling suggests photosynthesis is the major inducer of precipitation in thrombolite-forming mats.

In addition to the microbial and functional gene analyses, the stable isotope profiling provided new insights into the microbial nitrogen cycling and the mechanisms driving carbonate precipitation. Additionally, the SIMS approach enabled for one of the most highly spatially resolved carbonate oxygen and carbon isotopic datasets to date on modern thrombolites. Organic N isotope values approached 0‰, indicating nitrogen fixation was the dominant N source (Hoering and Ford, 1960; Minagawa and Wada, 1986; Sigman *et al*., 2009), which is consistent with the abundance of heterocystous cyanobacteria, such as *Dichothrix* sp., and numerous nitrogen fixing anoxygenic phototrophs identified in Zone 1 (Fig. 8). These results are also consistent with the high number of nitrogen fixation genes (e.g., *nifD, nifH, nifK*) recovered from the metagenome and metatranscriptome of the thrombolites (Mobberley *et al.,* 2015). Additionally, the enrichment of ammonia-oxidizing archaea and high number of recovered transcripts associated with ammonia monooxygenase (*amoA*; Mobberley et al., 2015) within the mat coupled with the low numbers of bacterial nitrification genes observed in both the predictive and whole shotgun libraries suggest that these archaeal chemolithotrophs may be playing an important role in controlling nitrification and the cycling of fixed nitrogen within the thrombolite-forming mats.

Analysis of $\delta^{18}O$ values by using both bulk and SIMS analyses did not provide evidence of an evaporative signal, the results of which suggest biologically induced precipitation. The high rates of photosynthesis within the thrombolite-forming mats (Myshrall *et al.,* 2010) coupled with the previously published observations that red algae distributed throughout the tufts of *Dichothrix* sp. filaments lack precipitates (Planavsky *et al.,* 2009) make it unlikely that non-biological processes, such as CO_2 degassing, are driving the precipitation within the thrombolites. The SIMS $\delta^{18}O$ values for filaments are highly depleted

compared to the values associated with the sediments, and previous studies have shown that increased ^{18}O depletion under elevated pH (Spero and Lea, 1996) is potentially suggestive of rapid rates of carbonate precipitation (McConnaughey, 1989). However, the offset between the bulk and SIMS $\delta^{18}O$ values cannot yet be fully explained, as systematically lower SIMS values have been observed up to 2‰ (Orland *et al*., 2015) and may be the product of water or organics within the sample site. Despite this potential, there is low variability in the $^{16}OH/^{16}O$ values (Supplemental Table S4), which suggests that the zonation revealed by the SIMS data is accurate. The difference between SIMS and bulk measurements may, in part, reflect the extensive grinding during sample preparation for bulk isotope analysis. Previous studies in corals have shown that the friction generated during milling or drilling of the carbonate samples can cause inversion of aragonite to calcite (Waite and Swart, 2015). As a result of extensive processing (e.g., milling), the $\delta^{18}O$ values cause correction errors from 0.2 ‰ per 1% of inversion from aragonite to calcite (Waite and Swart, 2015). Such differences between the two approaches reinforce the value of using a SIMS-based approach to capture the extensive variability that likely exists within the microenvironments of thrombolite forming mats.

The bulk $\delta^{13}C$ values of the organic matter associated within the thrombolites were heavy (mean -9.6 ± 0.2‰) relative to RuBisCO-mediated carbon fixation, which exhibits fractionations that typically span between -35 to -23‰ in both plant and microbial ecosystems and can be highly species-dependent (Farquhar *et al.*, 1989; Falkowski, 1991). The values also appear heavier than other known microbialite systems. For example, unlaminated nodules of Pavilion Lake exhibit a mean bulk organic $\delta^{13}C$ value of -26.8‰ (Brady *et al*., 2010) ,and microbialites in Cuatros Ciénegas range from -25‰ and -27‰ (Breitbart et al., 2009). These $\delta^{13}C$ –enriched values in the Bahamian thrombolites may reflect diffusion limitations of CO_2 into the intertidal microbialites, differences in light

intensities (Cooper and DeNiro, 1989), and the relatively high rates of photosynthesis (Myshrall *et al*., 2010). Values of organic $\delta^{13}C$ similar to the Bahamian thrombolites have been observed in microbial mats found in the hypersaline Solar Lake (-5.7 ± 1.4‰) and Gavish Sabkha (-10 ± 2.6‰) and have been attributed to EPS-rich materials on the surface of mats that impede transport of CO_2 into the mats (Schidlowski *et al.*, 1984). Previous studies have also shown that external factors, such as increased salinity and temperature, also decrease the solubility of CO_2 (Mucci, 1983). Therefore, the abundance of EPS material within the thrombolite-forming mats coupled with high rates of productivity (Myshrall *et al.,* 2010) may result in a potential shortage of CO_2 that may reduce isotopic discrimination of ^{13}C and is consistent with the idea of HCO_3 dissociation driving a pH shift and inducing carbonate precipitation.

The overall carbon isotope profiles of the carbonate suggest that the thrombolites of Highborne Cay are primarily the result of photoautotrophic carbon fixation, which correlates to several lacustrine microbialite systems, such as Lake Clifton, Pavilion Lake, Great Salt Lake, Green Lake, and Bacalar (for review see Chagas *et al*., 2016). The bulk isotope data for carbonates also correlates well with previous analyses on the *Dichothrix* calcified filaments (Planavsky *et al.,* 2009), as well as several lacustrine microbialites, such as Pavilion Lake (-1.2 – 2.3 ‰; Brady *et al*., 2010; Russell *et al*., 2014), Kelly Lake (4 – 5‰; Ferris *et al*., 1997), Lake Van (6‰), Lake Alchichia (6.5‰), and Great Salt Lake (4.2‰) (Chagas *et al*., 2016). Interestingly, the thrombolite measurements are also higher than the $\delta^{13}C$ values of the adjacent stromatolites located only a few meters away in the subtidal zone. The discrepancy may reflect the role of heterotrophic processes in carbonate precipitation in the Bahamian stromatolites (Andres *et al*., 2006), and similar results have been observed in the fresh water microbialites of Cuatros Ciénegas (Breitbart *et al.,* 2009) suggesting that

heterotrophic process may be also be influencing carbonate precipitation in the Mexican system.

Although SIMS data from Highborne Cay thrombolites show greater variability than bulk isotopes, the means are not statistically different. Some of the extensive variability in the SIMS $\delta^{13}C_{carb}$ values for filaments is tied to variations in the microenvironments along the vertically orientated cyanobacteria filaments. The lightest SIMS $\delta^{13}C$ values in filaments may reflect the presence of localized organics (e.g., EPS material) associated with the calcified filaments, given that organic carbon has higher ionization efficiency than carbonate. However, as SIMS threshold cutoffs were applied to eliminate any spots that might include organics, the lower $\delta^{13}C$ values likely accurately capture filament carbonate values. In contrast, the isotopically enriched samples, relative to values predicted from precipitation from local marine DIC, provide evidence for carbonate precipitation in a microenvironment influenced by carbon dioxide uptake, which increases the pH (Visscher *et al*., 1991, 1998, 2005; Planavsky *et al.,* 2009). The highest SIMS $\delta^{13}C$ values are more isotopically enriched than any previously reported Highborne Cay bulk thrombolite or filament $\delta^{13}C$ values (Planavsky *et al.,* 2009). Planavsky et al., (2009) used an offset between *Dichothrix* filament and detrital sediment $\delta^{13}C$ values to argue for photosynthetic carbon dioxide consumption as the initiation factor for carbonate precipitation within the filament sheaths. The observed markedly enriched filament $\delta^{13}C$ values strengthen the case for a photosynthetic carbonate precipitation trigger in the Bahamian thrombolites.

5. Conclusions

The integrated approaches of microbial diversity, metagenome prediction, microelectrode, and stable isotope analysis address several important gaps in our previous understanding of modern thrombolite-forming communities. This study provides a comprehensive spatial

portrait of thrombolite-forming communities revealing that, despite having unlaminated, clotted microstructures, these thrombolitic communities form distinct taxonomic and metabolic stratifications. Additionally, the SIMS results, the first ever generated for a microbialite-forming ecosystem, reveal SIMS $\delta^{13}C$ values that are more isotopically enriched than any previously reported bulk thrombolite values (Planavsky *et al*., 2009; Warden *et al*., 2016), providing direct evidence of a photosynthetic trigger for carbonate precipitation in the thrombolite-forming communities, which differs from stromatolites. Even within the same environment, where thrombolites are juxtaposed to stromatolites under similar environmental conditions (e.g., pH, salinity, temperature, UV flux), these differences between their taxa and metabolic activities appear to generate very distinct carbonate microstructures. Elucidating how these disparate structural fabrics arise will require a more detailed look into the networking and connectivity of the microbial interactions and metabolisms. Regulation of these processes on both diel and seasonal time scales will help assess the patterns associated with microbial activities and their response to their changing environment. Together, these analyses help elucidate the pathways associated with microbialite formation and represent a valuable tool to help reconstruct the microbiological and environmental conditions of the past.

Acknowledgements

The authors would like to thank Jennifer Larimore for her technical assistance. A.S.L was supported by the NSF Graduate Research Fellowship Program and J.M.M was supported by the NASA Graduate Student Research Program fellowship (NNX10AO18H). The research efforts were supported by the NASA Exobiology and Evolutionary Biology program element (NNX12AD64G). WiscSIMS is funded by NSF (EAR1355590).

Author Disclosure Statement

No competing financial interests exist

Author Contributions

A.L., J.M., R.R., P.V., and J.F. conceived the experiments. J.M., P.H., J.F., and P.V. collected the samples. All authors contributed to the performance and analysis of the experiments. All authors reviewed and approved the final manuscript.

References

Aitken JD. (1967) Classification and environmental significance of cryptalgal limestones and dolomites, with illustrations from the Cambrian and Ordovician of southwestern Alberta. *Journal of Sedimentary Petrology*, 37, 1163-1178.

Andres M, Sumner D, Reid RP, and Swart PK. (2006) Isotopic fingerprints of microbial respiration in aragonite from Bahamian stromatolites. *Geology*, 34, 973-976.

Andres MS, and Reid RP. (2006) Growth morphologies of modern marine stromatolites: a case study from Highborne Cay, Bahamas. *Sedimentary Geology*, 185, 319-328.

Arp G, Helms G, Kalinska K, Schumann G, Reimer A, Reitner J, and Trichet J. (2012) Photosynthesis versus exopolymer degradation in the formation of microbialites on the atoll of Kiritimati, Republic of Kiribati, Central Pacific. *Geomicrobiology Journal*, 29, 29-65.

Barns SM, Fundyga RE, Jeffries MW, and Pace NR. (1994) Remarkable archaeal diversity detected in a Yellowstone National Park hot spring environment. *Proceedings of the National Academy of Sciences*, 91, 1609-13.

Bernhard JM, Edgcomb VP, Visscher PT, McIntyre-Wressnig A, Summons RE, Bouxsein ML, Louis L, and Jeglinski M. (2013) Insights into foraminiferal influences on

microfabrics of microbialites at Highborne Cay, Bahamas. *Proceedings of the National Academy of Sciences*, 110, 9830-9834.

Bowlin EM, Klaus J, Foster JS, Andres M, Custals L, and Reid RP. (2012) Environmental controls on microbial community cycling in modern marine stromatolites. *Sedimentary Geology*, 263-264, 45-55.

Breitbart M, Hoare A, Nitti A, Siefert J, Haynes M, Dinsdale E, Edwards R, Souza V, Rohwer F, and Hollander D. (2009) Metagenomic and stable isotopic analyses of modern freshwater microbialites in Cuatro Ciénegas, Mexico. *Environmental Microbiology*, 11, 16-34.

Burne RV, and Moore LS. (1987) Microbialites: organosedimentary deposits of benthic microbial communities. *PALAIOS*, 2, 241-254.

Burns BP, Goh F, Allen M, and Neilan BA. (2004) Microbial diversity of extant stromatolites in the hypersaline marine environment of Shark Bay, Australia. *Environmental Microbiology*, 6, 1096-1101.

Calder JA, and Parker PL. (1973) Geochemical implocations of induced changes in ^{13}C fractionation by blue-green algae. *Geochimica et Cosmochimica Acta*, 37, 133-140.

Canfield DE, and Des Marais DJ. (1993) Biogeochemical cycles of carbon, sulfur, and free oxygen in a microbial mat. *Geochimica et Cosmochimica Acta*, 57, 3971-3984.

Caporaso JG, Kuczynski J, Stombaugh J, Bittinger K, Bushman FD, Costello EK, Fierer N, Pena AG, Goodrich JK, Gordon JI and others. (2010) QIIME allows analysis of high-throughput community sequencing data. *Nature Methods*, 7, 335-6.

Casaburi G, Duscher AA, Reid RP, and Foster JS. (2016) Characterization of the stromatolite microbiome from Little Darby Island, The Bahamas using predictive and whole shotgun metagenomic analysis. *Environmental Microbiology*, 18, 1452-1469.

Casamayor EO, Massana R, Benlloch S, Ovreas L, Diez B, Goddard VJ, Gasol JM, Joint I, Rodriguez-Valera F, and Pedros-Alio C. (2002) Changes in archaeal, bacterial and eukaryal assemblages along a salinity gradient by comparison of genetic fingerprinting methods in a multipond solar saltern. *Environmental Microbiology*, 4, 338-48.

Chagas AAP, Webb GE, Burne RA, and Southam G. (2016) Modern lacustrine mcirobialites; towards a synthesis of aquous and carbonate geochemistry and minerology. *Earth Science Reviews*, 162, 338-363.

Cooper LW, and DeNiro MJ. (1989) Stable carbon isotope variability in the seagrass *Posidonia oceanica*: evidence for light intensity effects. *Marine Ecology Progress Series*, 50, 225-229.

Dang H, Yang J, Li J, Luan X, Zhang Y, Gu G, Xue R, Zong M, and Klotz MG. (2013) Environment-dependent distribution of the sediment nifH-harboring microbiota in the Northern South China Sea. *Applied and Environmental Microbiology*, 79, 121-132.

Decho AW, Norman RS, and Visscher PT. (2010) Quorum sensing in natural environments: emerging views from microbial mats. *Trends in Microbiology*, 18, 73-80.

DeLong EF. (1992) Archaea in coastal marine environments. *Proceedings of the National Academy of Sciences*, 89, 5685-5689.

DeSantis TZ, Hugenholtz P, Larsen N, Rojas M, Brodie EL, Keller K, Huber T, Dalevi D, Hu P, and Andersen GL. (2006) Greengenes, a chimera-checked 16S rRNA gene database and workbench compatible with ARB. *Applied and Environmental Microbiology*, 72, 5069-5072.

Dravis JJ. (1983) Hardened subtidal stromatolites, Bahamas. *Science*, 219, 385-386.

Dridi B, Fardeau ML, Ollivier B, Raoult D, and Drancourt M. (2012) *Methanomassiliicoccus luminyensis* gen. nov., sp. nov., a methanogenic archaeon isolated from human faeces. *International Journal of Systematics and Evolutionary Microbiology*, 62, 1902-7.

Dupraz C, Reid RP, Braissant O, Decho AW, Norman RS, and Visscher PT. (2009) Processes of carbonate precipitation in modern microbial mats. *Earth Science Reviews*, 96, 141-162.

Dupraz C, and Visscher PT. (2005) Microbial lithification in marine stromatolites and hypersaline mats. *Trends in Microbiology*, 13, 429-438.

Dupraz C, Visscher PT, Baumgartner LK, and Reid RP. (2004) Microbe-mineral interactions: early carbonate precipitation in a hypersaline lake (Eleuthera Island, Bahamas). *Sedimentology*, 51, 1-21.

Edgcomb VP, Bernhard JM, Beaudoin D, Pruss S, Welander PV, Schubotz F, Mehay S, Gillespie AL, and Summons RE. (2013) Molecular indicators of microbial diversity in oolitic sands of Highborne Cay, Bahamas. *Geobiology*, 11, 234-251.

Falkowski PG. (1991) Species variability in the fractionation of ^{13}C and ^{12}C by marine phytoplankton. *Journal of Plankton Research*, 13, 21-28.

Farquhar GD, Ehleringer JR, and Hubick KT. (1989) Carbon isotope discrimination and photosynthesis. *Annual Review of Plant Physiology and Plant Molecular Biology*, 40, 503-537.

Feist AM, Scholten JC, Palsson BO, Brockman FJ, and Ideker T. (2006) Modeling methanogenesis with a genome-scale metabolic reconstruction of *Methanosarcina barkeri*. *Molecular System Biology*, 2, 1.

Ferris FG, Thompson JB, and Beveridge TJ. (1997) Modern freshwater microbialites from Kelly Lake, British Columbia, Canada. *PALAIOS*, 12, 213-219.

Foster JS, and Green SJ. (2011) Microbial diversity in modern stromatolites In: *Cellular Origin, Life in Extreme Habitats and Astrobiology: Interactions with Sediments*. edited by J Seckbach and V Tewaris, Springer, p 385-405.

Gallagher KL, Kading TJ, Braissant O, Dupraz C, and Visscher PT. (2012) Inside the alkalinity engine: The role of electron donors in the organomineralization potential of sulfate-reducing bacteria. *Geobiology*, 10, 518-530.

Glunk C, Dupraz C, Braissant O, Gallagher KL, Verrecchia EP, and Visscher PT. (2011) Microbially mediated carbonate precipitation in a hypersaline lake, Big Pond (Elutera, Bahamas). *Sedimentology*, 58, 720-738.

Green SJ, Blackford C, Bucki P, Jahnke LL, and Prufert-Bebout L. (2008) A salinity and sulfate manipulation of hypersaline microbial mats reveals stasis in the cyanobacterial community structure. *ISME Journal*, 2, 457-470.

Hester ER, Barott KL, Nulton J, Vermeij NJA, and Rohwer FL. (2016) Stable and sporadic symbiotic communities of coral and algal holobionts. *ISME Journal*, 10, 1157-1169.

Hoering T, and Ford HT. (1960) The isotope effect in the fixation of nitrogen by *Azotobacter*. *Journal of American Chemical Society*, 82, 376-378.

Houghton J, Fike D, Druschel G, Orphan V, Hoehler TM, and Des Marais DJ. (2014) Spatial variability in photosynthetic and heterotrophic activity drives localized delta13C org fluctuations and carbonate precipitation in hypersaline microbial mats. *Geobiology*, 12, 557-74.

Huson DH, Auch AF, Qi J, and Schuster SC. (2007) MEGAN analysis of metagenomic data. *Genome Research*, 17, 377-386.

Iino T, Tamaki H, Tamazawa S, Ueno Y, Ohkuma M, Suzuki K, Igarashi Y, and Haruta S. (2013) Candidatus *Methanogranum caenicola*: a novel methanogen from the anaerobic digested sludge, and proposal of Methanomassiliicoccaceae fam. nov. and

Methanomassiliicoccales ord. nov., for a methanogenic lineage of the class Thermoplasmata. *Microbes and Environments*, 28, 244-50.

Kanehisa M, and Goto S. (2000) KEGG: kyoto encyclopedia of genes and genomes. *Nucleic Acids Research*, 28, 27-30.

Kennard JM, and James NP. (1986) Thrombolites and stromatolites: two distinct types of microbial structures. *PALAIOS*, 1, 492-503.

Kenward PA, Goldstein RH, Gonzalez LA, and Roberts JA. (2009) Precipitation of low-temperature dolomite from an anaerobic microbial consortium: the role of methanogenic Archaea. *Geobiology*, 7, 556-565.

Khodadad CL, and Foster JS. (2012) Metagenomic and metabolic profiling of nonlithifying and lithifying stromatolitic mats of Highborne Cay, The Bahamas. *PLoS ONE*, 7, e38229.

Kita NT, Huberty JM, Kozdon R, Beard BL, and Valley JW. (2011) High-precision SIMS oxygen, sulfur and iron stable isotope analyses of geological materials: accuracy, surface topography and crystal orientation. *Surface and Interface Analysis*, 43, 427-431.

Kozdon R, Kelly DC, Kita NT, Fournelle JH, and Valley JW. (2011) Planktonic foraminiferal oxygen isotope analysis by ion microprobe technique suggests warm tropical sea surface temperatures during the Early Paleogene. *Paleoceanography*, 26.

Kozdon R, Ushikubo T, Kita NT, Spicuzza M, and Valley JW. (2009) Intratest oxygen isotope cariability in the planktonic foraminifer *N. pachyderma*: real versus apparent vital effects by ion microprobe. *Chemical Geology*, 258, 327-337.

Krekeler D, Teske AP, and Cypionka H. (1997) Strategies of sulfate-reducing bacteria to escape oxygen stress in a cyanobacterial mat. *FEMS Microbiology Ecology*, 25, 89-96.

Landini P, and Zehnder AJ. (2002) The global regulatory *hns* gene negatively affects adhesion to solid surfaces by anaerobically grown *Escherichia coli* by modulating expression of flagellar genes and lipopolysaccharide production. *Journal of Bacteriology*, 184, 1522-9.

Langille MG, Zaneveld J, Caporaso JG, McDonald D, Knights D, Reyes JA, Clemente JC, Burkepile DE, Vega Thurber RL, Knight R and others. (2013) Predictive functional profiling of microbial communities using 16S rRNA marker gene sequences. *Nature Biotechnology*, 31, 814-821.

Laval B, Cady SL, Pollack JC, McKay CP, Bird JS, Grotzinger JP, Ford DC, and Bohm HR. (2000) Modern freshwater microbialite analogues for ancient dendritic reef structures. *Nature*, 407, 626-629.

Lenk S, Arnds J, Zerjatke K, Musat N, Amann R, and Mussmann M. (2011) Novel groups of Gammaproteobacteria catalyse sulfur oxidation and carbon fixation in a coastal, intertidal sediment. *Environmental Microbiology*, 13, 758-774.

Linzmeier B, Kozdon R, Peters S, and Valley JW. (2016) Oxygen isotope variability within growth bands suggests daily depth migration behavior is recorded in *Nautilus* shell aragonite. *PLoS ONE*, e0153890.

Logan BW. (1961) *Crytpzoan* and associated stromatolties from the recent, Shark Bay, Western Australia. *Journal of Geology*, 69, 517-533.

Lozupone C, and Knight R. (2005) UniFrac: a new phylogenetic method for comparing microbial communities. *Applied and Environmental Microbiology*, 71, 8228-8235.

McConnaughey T. (1989) ^{13}C and ^{18}O isotopic disequilibrium in biological carbonates: I. Patterns. *Geochimica et Cosmochimica Acta*, 53, 151-162.

Minagawa M, and Wada E. (1986) Nitrogen isotope ratios fo red tide organisms in the East China Sea: a characterization of biological nitrogen fixation. *Marine Chemistry*, 19, 245-259.

Minz D, Fishbain S, Green SJ, Muyzer G, Cohen Y, Rittmann BE, and Stahl DA. (1999) Unexpected population distribution in a microbial mat community: sulfate-reducing bacteria localized to the highly oxic chemocline in contrast to a eukaryotic preference for anoxia. *Applied and Environmental Microbiology*, 65, 4659-4665.

Mobberley JM, Khodadad CL, and Foster JS. (2013) Metabolic potential of lithifying cyanobacteria-dominated thrombolitic mats. *Photosynthesis Research*, 118, 125-140.

Mobberley JM, Khodadad CL, Visscher PT, Reid RP, Hagan P, and Foster JS. (2015) Inner workings of thrombolites: spatial gradients of metabolic activity as revealed by metatranscriptome profiling. *Scientific Reports*, 5, 12601.

Mobberley JM, Ortega MC, and Foster JS. (2012) Comparative microbial diversity analyses of modern marine thrombolitic mats by barcoded pyrosequencing. *Environmental Microbiology*, 14, 82-100.

Mucci A. (1983) The solubility of calcite and aragonite in seawater at various salinities, temperatures, and one atmosphere total pressure. *American Journal of Science*, 283, 780-799.

Myshrall K, Mobberley JM, Green SJ, Visscher PT, Havemann SA, Reid RP, and Foster JS. (2010) Biogeochemical cycling and microbial diversity in the modern marine thrombolites of Highborne Cay, Bahamas. *Geobiology*, 8, 337-354.

Ondov BD, Bergman NH, and Phillippy AM. (2011) Interactive metagenomic visualization in a Web browser. *BMC Bioinformatics*, 12, 385.

Orland IJ. (2012) Seasonality from speleothems: high-resolution ion microprobe studies at Soreq Cave, Israel: University of Wisconsin-Madison.

Orland IJ, Bar-Matthews M, Kita NT, Ayalon A, Matthews A, and Valley JW. (2009) Climate deterioration in the Eastern Mediterranean as revealed by ion microprobe analysis of a speleothem that grew from 2.2 to 0.9 ka in Soreq Cave, Israel. *Quaternary Research*, 71, 27-35.

Pages A, Welsh DT, Teasdale PR, Grice K, Vacher M, Bennett WW, and Visscher PT. (2014) Diel fluctuations in solute distributions and biogeochemical cycling in a hypersaline microbial mat from Shark Bay, WA. *Marine Chemistry*, 167, 102-112.

Paul VG, Wronkiewicz DJ, Mormile MR, and Foster JS. (2016) Mineralogy and microbial diversity of the microbialites in the hypersaline Storr's Lake, The Bahamas. *Astrobiology*, 16, 282-300.

Petrash DA, Gingras MK, Lalonde SV, Orange F, Pecoits E, and Konhauser KO. (2012) Dynamic controls on accretion and lithification on modern gypsum-dominated thrombolites, Los Roques, Venezuela. *Sedimentary Geology*, 245-246, 29-47.

Pfennig N, and Trüper HG. (1992) The family Chromatiaceae. In: *The Prokaryotes*, Springer, New York, p 3200-3221.

Planavsky N, and Ginsburg RN. (2009) Taphonomy of modern marine Bahamian microbialites. *PALAIOS*, 24, 5-17.

Planavsky N, Reid RP, Andres M, Visscher PT, Myshrall KL, and Lyons TW. (2009) Formation and diagenesis of modern marine calcified cyanobacteria. *Geobiology*, 7, 566-576.

Poulsen M, Schwab C, Jensen BB, Engberg RM, Spang A, Canibe N, Hojberg O, Milinovich G, Fragner L, Schleper C and others. (2013) Methylotrophic methanogenic Thermoplasmata implicated in reduced methane emissions from bovine rumen. *Nature Communication*, 4, 1428.

Price MN, Dehal PS, and Arkin AP. (2010) FastTree 2--approximately maximum-likelihood trees for large alignments. *PLoS ONE*, 5, e9490.

Reid RP, Macintyre IG, and Steneck RS. (1999) A microbialite/algal-ridge fringing reef complex, Highborne Cay, Bahamas. *Atoll Research Bulletin*, 465, 459-465.

Reid RP, Visscher PT, Decho AW, Stolz JF, Bebout BM, Dupraz C, Macintyre IG, Paerl HW, Pinckney JL, Prufert-Bebout L and others. (2000) The role of microbes in accretion, lamination and early lithification of modern marine stromatolites. *Nature*, 406, 989-992.

Risatti JB, Capman WC, and Stahl DA. (1994) Community structure of a microbial mat: the phylogenetic dimension. *Proceedings of the National Academy of Sciences*, 91, 10173-10177.

Russell JA, Brady AL, Cardman Z, Slater GF, Lim DS, and Biddle JF. (2014) Prokaryote populations of extant microbialites along a depth gradient in Pavilion Lake, British Columbia, Canada. *Geobiology*, 12, 250-64.

Ruvindy R, White III, RA, Neilan BA, and Burns BP. (2016) Unravelling core microbial metabolisms in the hypersaline microbial mats of Shark Bay using high-throughput metagenomics. *ISME Journal*, 10, 183-196.

Sabra W, Lunsdorf H, and Zeng AP. (2003) Alterations in the formation of lipopolysaccharide and membrane vesicles on the surface of *Pseudomonas aeruginosa* PAO1 under oxygen stress conditions. *Microbiology*, 149, 2789-95.

Saghaï A, Zivanovic Y, Zeyen N, Moreira D, Benzerara K, Deschamps P, Bertolino P, Ragon M, Tavera R, Lopez-Archilla AI and others. (2015) Metagenome-based diversity analyses suggest a significant contribution of non-cyanobacterial lineages to carbonate precipitation in modern microbialites. *Frontiers in Microbiology*, 6, 797.

Schidlowski M, and Matzigkeit U. (1984) Superheavy organic carbon from hypersaline microbial mats. *Naturwissenschaften*, 71, 303-308.

Schneider D, Arp G, Reimer A, Reitner J, and Daniel R. (2013) Phylogenetic analysis of a microbialite-forming microbial mat from a hypersaline lake of the Kiritimati atoll, Central Pacific. *PLoS ONE*, 8, e66662.

Sigman DM, Karsh KL, and Casciotti KL. (2009) Ocean process tracers: nitrogen isotopes in the ocean. *Encyclopedia of Ocean Science*, 4138-4153.

Spero HJ, and Lea DW. (1996) Experimental determination of stable isotope variability in *Globigerina bulloides*: implications for paleoceanographic reconstructions. *Marine Micropaleontology*, 28, 231-246.

Stolz JF, Reid RP, Visscher PT, Decho AW, Norman RS, Aspden RJ, Bowlin EM, Franks J, Foster JS, Paterson DM and others. (2009) The microbial communities of the modern marine stromatolites at Highborne Cay, Bahamas. *Atoll Research Bulletin*, 567, 1-29.

Suosaari EP, Reid RP, Playford PE, Foster JS, Stolz JF, Casaburi G, Hagan PD, Chirayath V, Macintyre IG, Planavsky NJ and others. (2016) New multi-scale perspectives on the stromatolites of Shark Bay, Western Australia. *Scientific Reports*, 6, 20557.

Swart PK, and Eberli GP. (2005) The nature of the δ13C of periplatform sediments: Implications for stratigraphy and the global carbon cycle. *Sedimentary Geology*, 175, 115-129.

Valdespino-Castillo PM, Alcantara-Hernandez RJ, Alcocer J, Merino-Ibarra M, Macek M, and Falcon LI. (2014) Alkaline phosphatases in microbialites and bacterioplankton from Alchichica soda lake, Mexico. *FEMS Microbiology Ecology*, 90, 504-19.

Valley JW, and Kita NT. (2009) In situ oxygen isotope geochemistry by ion microprobe. In: *Mineralogical Association of Canada Short Course*, p 19-63.

Vazquez-Baeza Y, Pirrung M, Gonzalez A, and Knight R. (2013) EMPeror: a tool for visualizing high-throughput microbial community data. *Gigascience*, 2, 16.

Vetter L, Kozdon R, Valley JW, Mora CI, and Spero HJ. (2014) SIMS measurements of intrashell $\delta^{13}C$ in the cultured planktic foraminifer *Orbulina universa*. *Geochimica et Cosmochimica Acta*, 139.

Visscher PT, Beukema J, and van Gemerden H. (1991) In situ characterization of sediments: measurement of oxygen and sulfide profiles with a novel combined needle electrode. *Limnology and Oceanography*, 36, 1476-1480.

Visscher PT, Prins RA, and van Gemerden H. (1992) Rates of sulfate reduction and thiosulfate consumption in a marine microbial mat. *FEMS Microbiology Letters*, 86, 283-293.

Visscher PT, Reid RP, and Bebout BM. (2000) Microscale observations of sulfate reduction: correlation of microbial activity with lithified micritic laminae in modern marine stromatolites. *Geology*, 28, 919-922.

Visscher PT, Reid RP, Bebout BM, Hoeft SE, Macintyre IG, and Thompson JA. (1998) Formation of lithified micritic laminae in modern marine stromatolites (Bahamas): The role of sulfur cycling. *American Mineralogist*, 83, 1482-1493.

Visscher PT, and Stolz JF. (2005) Microbial mats as bioreactors: populations, processes and products. *Palaeogeography, Palaeoclimatology, Palaeoecology*, 219, 87-100.

Waite AJ, and Swart PK. (2015) The inversion of aragonite to calcite during the sampling of skeletal archives: implications for proxy interpretation. *Rapid Communications in Mass Spectrometry*, 29, 955-964.

Warden JG, Casaburi G, Omelon CR, Bennett PC, Breecker DO, and Foster JS. (2016) Characterization of microbial mat microbiomes in the modern thrombolite ecosystem

of Lake Clifton, Western Australia using shotgun metagenomics. *Frontiers in Microbiology*, 7, 1064.

White RA, 3rd, Chan AM, Gavelis GS, Leander BS, Brady AL, Slater GF, Lim DS, and Suttle CA. (2016) Metagenomic Analysis Suggests Modern Freshwater Microbialites Harbor a Distinct Core Microbial Community. *Frontiers in Microbiology*, 6, 1531.

White RA, 3rd, Power IM, Dipple GM, Southam G, and Suttle CA. (2015) Metagenomic analysis reveals that modern microbialites and polar microbial mats have similar taxonomic and functional potential. *Frontiers in Microbiology*, 6, 966.

Wickham H. (2009) ggplot2: elegant graphics for data analysis. Springer Science & Business Media.

Williford KH, Ushikubo T, Lepot K, Kitajima K, Hallmann C, Spicuzza MJ, Kozdon R, Eigenbrode JL, Summons RE, and Valley JW. (2016) Carbon and sulfur isotopic signatures of ancient life and environment at the microbial scale: Neoarchean shales and carbonates. *Geobiology*, 14, 105-128.

Wong HL, Smith DL, Visscher PT, and Burns BP. (2015) Niche differentiation of bacterial communities at a millimeter scale in Shark Bay microbial mats. *Scientific Reports*, 5, 15607.

Figure Legends

FIG. 1. The thrombolites of Highborne Cay, The Bahamas. **(A)** Intertidal thrombolite platforms from Site 5. Bar, 1 m. **(B)** Light micrograph of a thrombolite forming button mat revealing extensive vertical assemblages of calcified filaments (arrows). Bar, 500 μm. **(C)** *In situ* depth profiles of oxygen (square), sulfide (triangle), and pH (circle) collected at peak of photosynthesis (open symbols) or respiration (filled symbols). Shaded areas reflect the targeted areas collected for analysis. Depths below 9 cm were not sampled, as that region

shared the same biochemical profile as in Zone 3. **(D)** Cross section of button mat depicting the three spatial regions including an oxic Zone 1 (0 – 3 mm), transitional Zone 2 (3 – 5 mm), and anoxic Zone 3 (5 – 9 mm). Bar, 3 mm.

FIG. 2. Taxonomic distribution of cyanobacteria within the thrombolite-forming mats derived from MEGAN5 using the Greengenes database. Overall percentages based on read counts are presented logarithmically depicting the distributions for Zone 1 (blue), Zone 2 (green), and Zone 3 (red). Read abundance data for each taxonomic level are included in parentheses.

FIG. 3. Taxonomic distribution of Bacteria within the thrombolite-forming mats derived from MEGAN5 using the Greengenes database. Overall percentages based on read counts are presented logarithmically depicting the distributions for Zone 1 (blue), Zone 2 (green), and Zone 3 (red). Read abundance data for each taxonomic level are included in parentheses.

FIG. 4. Comparison of diversity analyses of three spatial zone within the thrombolite-forming mats. Principal coordinate analysis of communities from unweighted UniFrac distance matrix of Zone 1 (0 – 3 mm, blue), Zone 2 (3 – 5 mm, green), and Zone 3 (5 – 9 mm, red) in **(A)** Bacteria and **(B)** Archaea populations. Ellipses represent standard deviation over ten rarefaction samplings. Adonis tests suggest that depth is a significant predictor of community composition for both bacterial ($R=0.402$, $p=0.001$) and archaeal ($R=0.307$, $p=0.017$) communities.

FIG. 5. Taxonomic distribution of Archaea within the thrombolite-forming mats derived from MEGAN5 using the Greengenes database. Overall percentages based on read counts are

presented logarithmically depicting the distributions for Zone 1 (blue), Zone 2 (green), and Zone 3 (red). Read abundance data for each taxonomic level are included in parentheses.

FIG. 6. Functional gene comparison of the three thrombolitic mat spatial zones from 16S rRNA metabolic prediction (PICRUSt) and whole shotgun sequencing. Pearson correlation value (r) is shown for the comparison of metabolic predictions for Zone 1 (blue), Zone 2 (green), and Zone 3 (red) and the whole mat shotgun metagenome.

FIG 7. Stable isotope results for calcified filaments located in the upper 3 mm of thrombolite forming button mat. **(A)** Oxygen isotope values of organic and inorganic fractions using both bulk and SIMS analysis. Analyses were completed for both background carbonate precipitates (sediment), calcified filaments (filaments) and untreated whole mat samples. **(B)** Carbon and nitrogen isotope values of both organic and inorganic fractions using both bulk and secondary ion mass spectroscopy (SIMS) analysis. **(C)** Comparative plot of SIMS values collected for oxygen and carbon isotopes. All results are expressed in delta notation with respect to the carbon/oxygen Vienna Peedee Belemnite (VPDB) or nitrogen air (AIR) standard.

FIG. 8. Overview of target areas for SIMS analyses within the thrombolite forming mat. **(A)** Petrographic thin section of *Dichothrix* sp. filaments (f) and associated carbonate precipitate (cp) surrounded by sediments such as ooids (o). **(B)** Gold-coated reflected light image as viewed by the SIMS instrument. **(C)** SEM micrograph showing the numerous 6-10 μm pits formed during the SIMS analysis. Boxes depict representative pits that show both high (green) and low (red) quality targets within the sample. **(D)** Higher resolution SEM micrograph of representative high quality pit (corresponding to green box in C) showing no

textural anomalies or cracks. **(E)** SEM micrograph of low quality pit (corresponding to red box in C) showing crack within the targeted sample site. All low quality target sites were removed from down-stream analyses.

Supplemental FIG. S1. Rarefaction plots for number of observed species approaching asymptote at read cutoffs of **(A)** 3691 for Bacteria and **(B)** 3587 for Archaea. Error bars represent standard deviation of three biological replicates for Zone 1 (0 – 3 mm, blue), Zone 2 (3 – 5 mm, green) and Zone 3 (5 – 9 mm, red).

Supplemental FIG. S2. Relative abundance of bacterial population. Lines depict family-level OTU (97% cutoff) differences between depth zones grouped by phylum. Taxonomy was assigned using the Greengenes database and filtered by abundance (0.005%).

Supplemental FIG. S3. Taxonomic abundance diversity of bacteria associated with Zone 1 (0 - 3 mm) of the thrombolite forming mats as visualized in a hierarchal Krona plot. Each ring within the plot represents a different taxonomic level (i.e., phylum, class, order, family). Taxa comprising less than 0.1% of the community were omitted.

Supplemental FIG. S4. Taxonomic abundance diversity of bacteria associated with Zone 2 (3 - 5 mm) of the thrombolites as visualized in a hierarchal Krona plot. Each ring within the plot represents a different taxonomic level (i.e., phylum, class, order, family). Taxa comprising less than 0.1% of the community were omitted.

Supplemental FIG S5. Taxonomic abundance diversity of bacteria associated with Zone 3 (5 - 9 mm) of the thrombolites as visualized in a hierarchal Krona plot. Each ring within the

plot represents a different taxonomic level (i.e., phylum, class, order, family). Taxa comprising less than 0.1% of the community were omitted.

Supplementary Table S1. Primer list used to generate titanium 454 barcoded libraries for bacteria and archaea.

Supplemental Table S2. Functional gene complexity of predicted and whole shotgun metagenome in the thrombolite forming mats of Highborne Cay, The Bahamas. (please note this table format is an excel worksheet but had to be uploaded as csv file).

Supplemental Table S3. Percent of key elements by weight found in the thrombolite-forming microbial mat.

Supplemental Table S4: Ion microprobe raw and corrected oxygen isotope ratios from 77 analyses of thrombolite samples 10B1 and 10B2 from Highborne Cay, The Bahamas. (Please note this table format is excel worksheet but had to be uploaded as two page csv file).

Supplemental Table S5: Ion microprobe raw and corrected carbon isotope ratios from 92 analyses of thrombolite samples 10B1 and 10B2 from Highborne Cay, The Bahamas. (Please note this table format is excel worksheet but had to be uploaded as two page pcsv file).

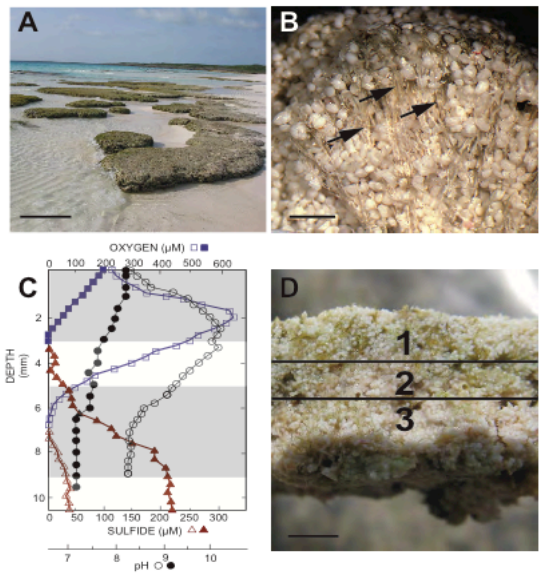
A
B
C
D
OXYGEN (µM)
0 100 200 300 400 500 600
DEPTH (mm)
2
4
6
8
10
0 50 100 150 200 250 300
SULFIDE (µM)
7 8 9 10
pH
1
2
3

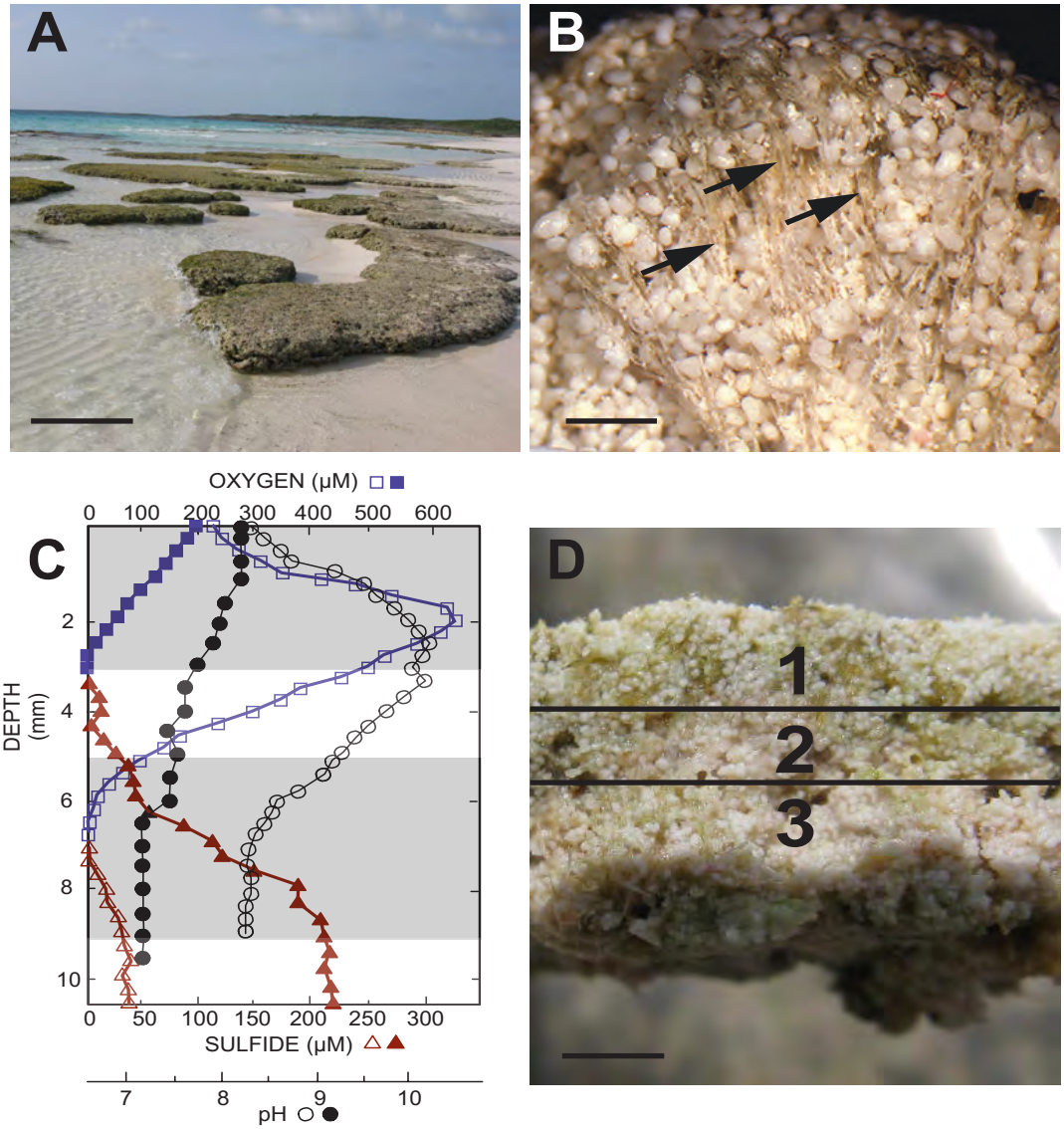
A
B
C
OXYGEN (μM)
0 100 200 300 400 500 600
DEPTH (mm)
2
4
6
8
10
0 50 100 150 200 250 300
SULFIDE (μM)
7 8 9 10
pH
D
1
2
3

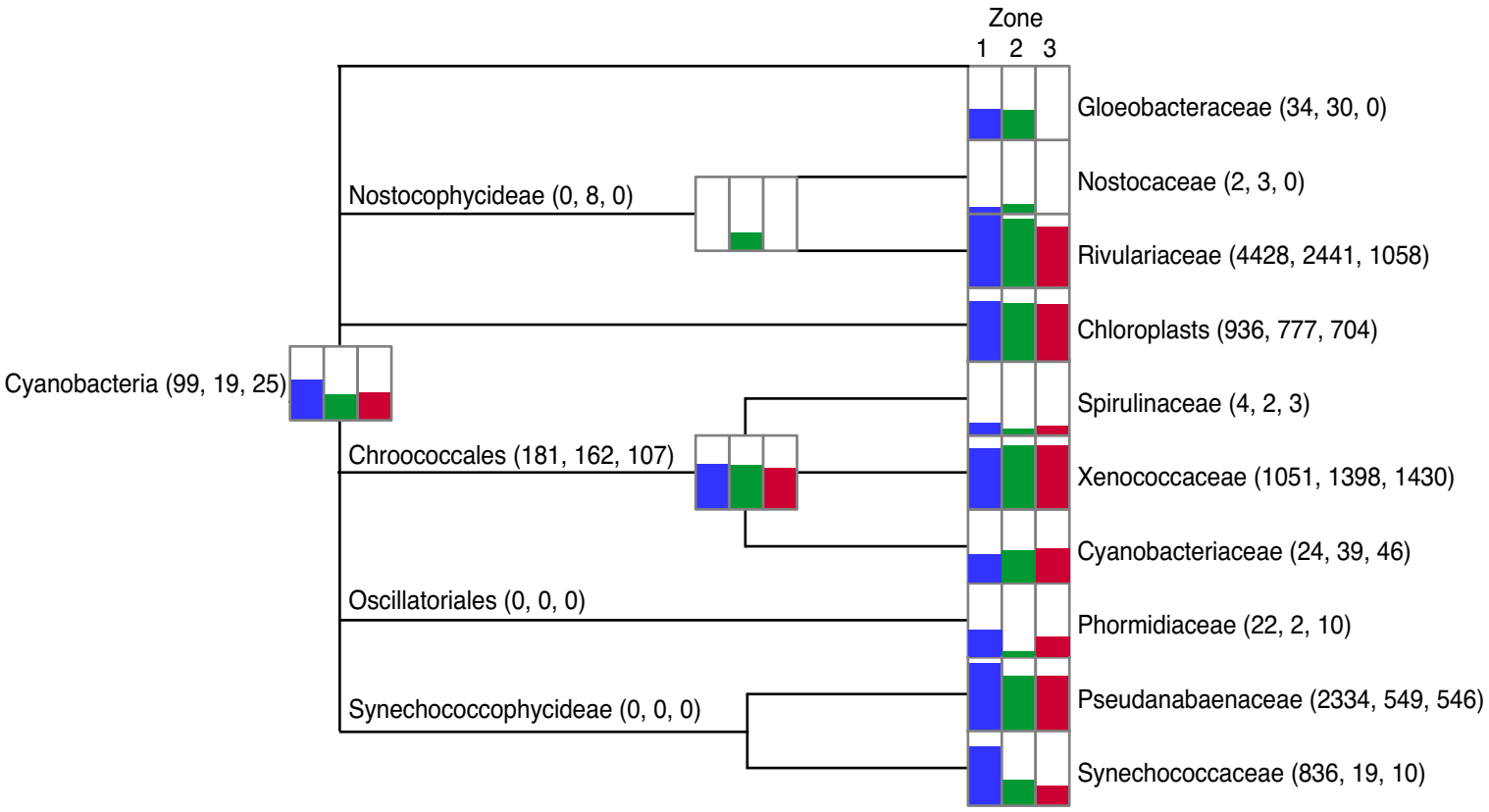
Zone
1 2 3
Gloeobacteraceae (34, 30, 0)
Nostocaceae (2, 3, 0)
Rivulariaceae (4428, 2441, 1058)
Chloroplasts (936, 777, 704)
Spirulinaceae (4, 2, 3)
Xenococcaceae (1051, 1398, 1430)
Cyanobacteriaceae (24, 39, 46)
Phormidiaceae (22, 2, 10)
Pseudanabaenaceae (2334, 549, 546)
Synechococcaceae (836, 19, 10)
Nostocophycideae (0, 8, 0)
Chroococcales (181, 162, 107)
Oscillatoriales (0, 0, 0)
Synechococcophycideae (0, 0, 0)
Cyanobacteria (99, 19, 25)

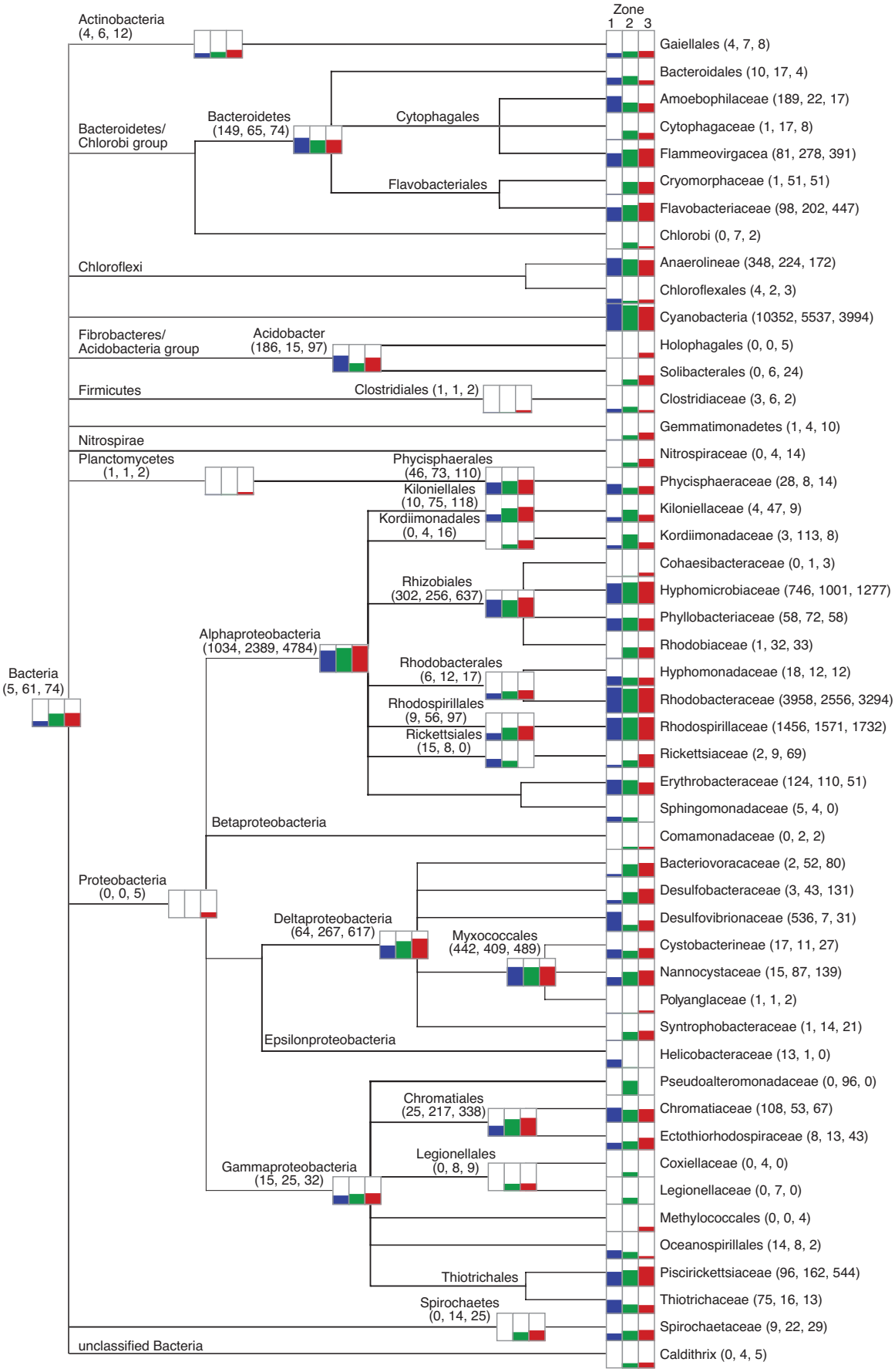
Zone
1 2 3
Actinobacteria
(4, 6, 12)
Bacteroidetes/
Chlorobi group
Bacteroidetes
(149, 65, 74)
Cytophagales
Flavobacteriales
Chloroflexi
Fibrobacteres/
Acidobacteria group
Acidobacter
(186, 15, 97)
Firmicutes
Clostridiales (1, 1, 2)
Nitrospirae
Planctomycetes
(1, 1, 2)
Phycisphaerales
(46, 73, 110)
Kiloniellales
(10, 75, 118)
Kordiimonadales
(0, 4, 16)
Rhizobiales
(302, 256, 637)
Alphaproteobacteria
(1034, 2389, 4784)
Rhodobacterales
(6, 12, 17)
Rhodospirillales
(9, 56, 97)
Rickettsiales
(15, 8, 0)
Bacteria
(5, 61, 74)
Betaproteobacteria
Proteobacteria
(0, 0, 5)
Deltaproteobacteria
(64, 267, 617)
Myxococcales
(442, 409, 489)
Epsilonproteobacteria
Chromatiales
(25, 217, 338)
Legionellales
(0, 8, 9)
Gammaproteobacteria
(15, 25, 32)
Thiotrichales
Spirochaetes
(0, 14, 25)
unclassified Bacteria
Gaiellales (4, 7, 8)
Bacteroidales (10, 17, 4)
Amoebophilaceae (189, 22, 17)
Cytophagaceae (1, 17, 8)
Flammeovirgacea (81, 278, 391)
Cryomorphaceae (1, 51, 51)
Flavobacteriaceae (98, 202, 447)
Chlorobi (0, 7, 2)
Anaerolineae (348, 224, 172)
Chloroflexales (4, 2, 3)
Cyanobacteria (10352, 5537, 3994)
Holophagales (0, 0, 5)
Solibacterales (0, 6, 24)
Clostridiaceae (3, 6, 2)
Gemmatimonadetes (1, 4, 10)
Nitrospiraceae (0, 4, 14)
Phycisphaeraceae (28, 8, 14)
Kiloniellaceae (4, 47, 9)
Kordiimonadaceae (3, 113, 8)
Cohaesibacteraceae (0, 1, 3)
Hyphomicrobiaceae (746, 1001, 1277)
Phyllobacteriaceae (58, 72, 58)
Rhodobiaceae (1, 32, 33)
Hyphomonadaceae (18, 12, 12)
Rhodobacteraceae (3958, 2556, 3294)
Rhodospirillaceae (1456, 1571, 1732)
Rickettsiaceae (2, 9, 69)
Erythrobacteraceae (124, 110, 51)
Sphingomonadaceae (5, 4, 0)
Comamonadaceae (0, 2, 2)
Bacteriovoracaceae (2, 52, 80)
Desulfobacteraceae (3, 43, 131)
Desulfovibrionaceae (536, 7, 31)
Cystobacterineae (17, 11, 27)
Nannocystaceae (15, 87, 139)
Polyanglaceae (1, 1, 2)
Syntrophobacteraceae (1, 14, 21)
Helicobacteraceae (13, 1, 0)
Pseudoalteromonadaceae (0, 96, 0)
Chromatiaceae (108, 53, 67)
Ectothiorhodospiraceae (8, 13, 43)
Coxiellaceae (0, 4, 0)
Legionellaceae (0, 7, 0)
Methylococcales (0, 0, 4)
Oceanospirillales (14, 8, 2)
Piscirickettsiaceae (96, 162, 544)
Thiotrichaceae (75, 16, 13)
Spirochaetaceae (9, 22, 29)
Caldithrix (0, 4, 5)

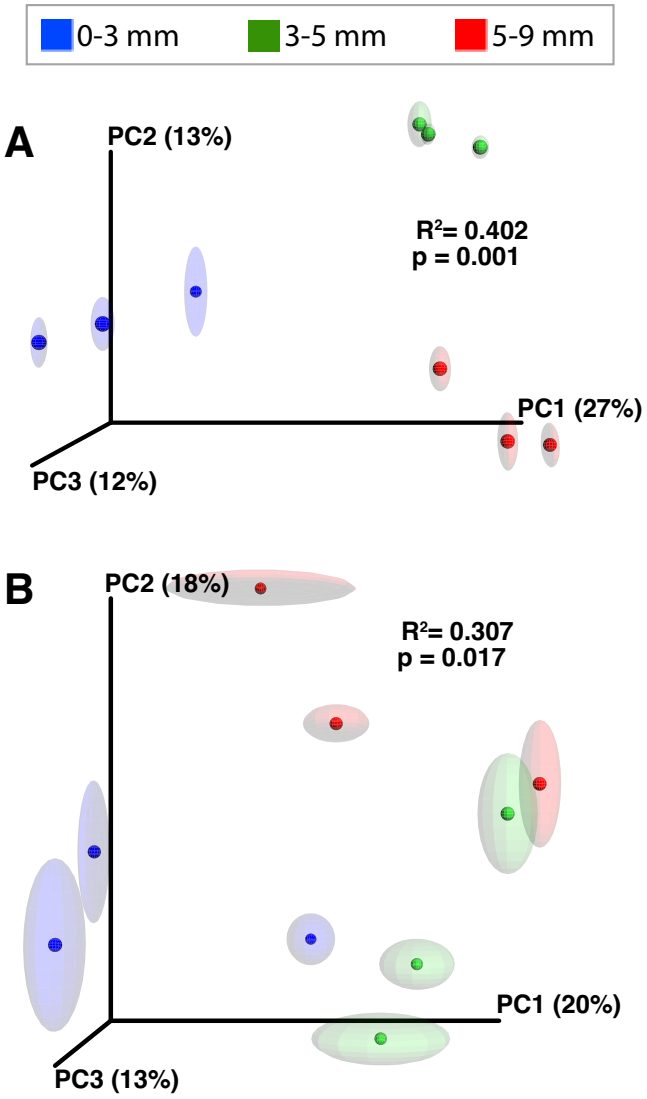
0-3 mm
3-5 mm
5-9 mm
A
PC2 (13%)
R²= 0.402
p = 0.001
PC1 (27%)
PC3 (12%)
B
PC2 (18%)
R²= 0.307
p = 0.017
PC1 (20%)
PC3 (13%)

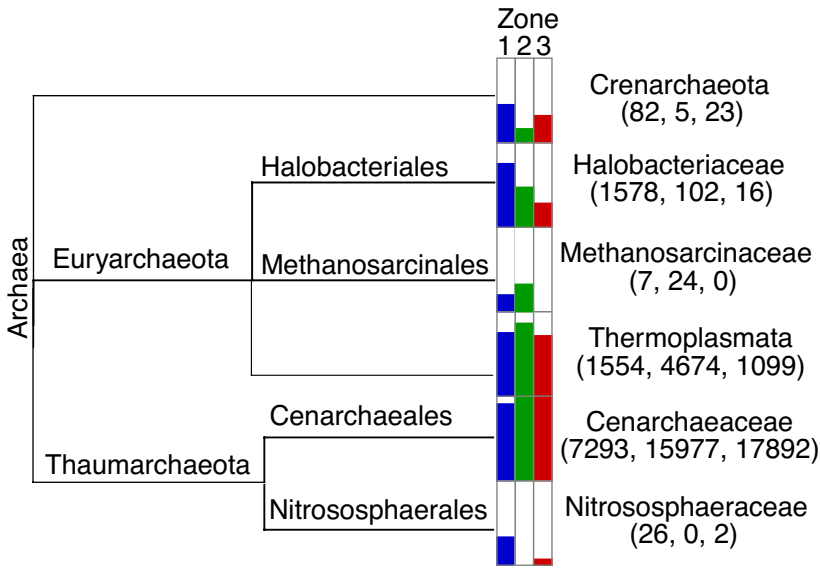
Zone
1 2 3
Archaea
Euryarchaeota
Thaumarchaeota
Halobacteriales
Methanosarcinales
Cenarchaeales
Nitrososphaerales
Crenarchaeota
(82, 5, 23)
Halobacteriaceae
(1578, 102, 16)
Methanosarcinaceae
(7, 24, 0)
Thermoplasmata
(1554, 4674, 1099)
Cenarchaeaceae
(7293, 15977, 17892)
Nitrososphaeraceae
(26, 0, 2)

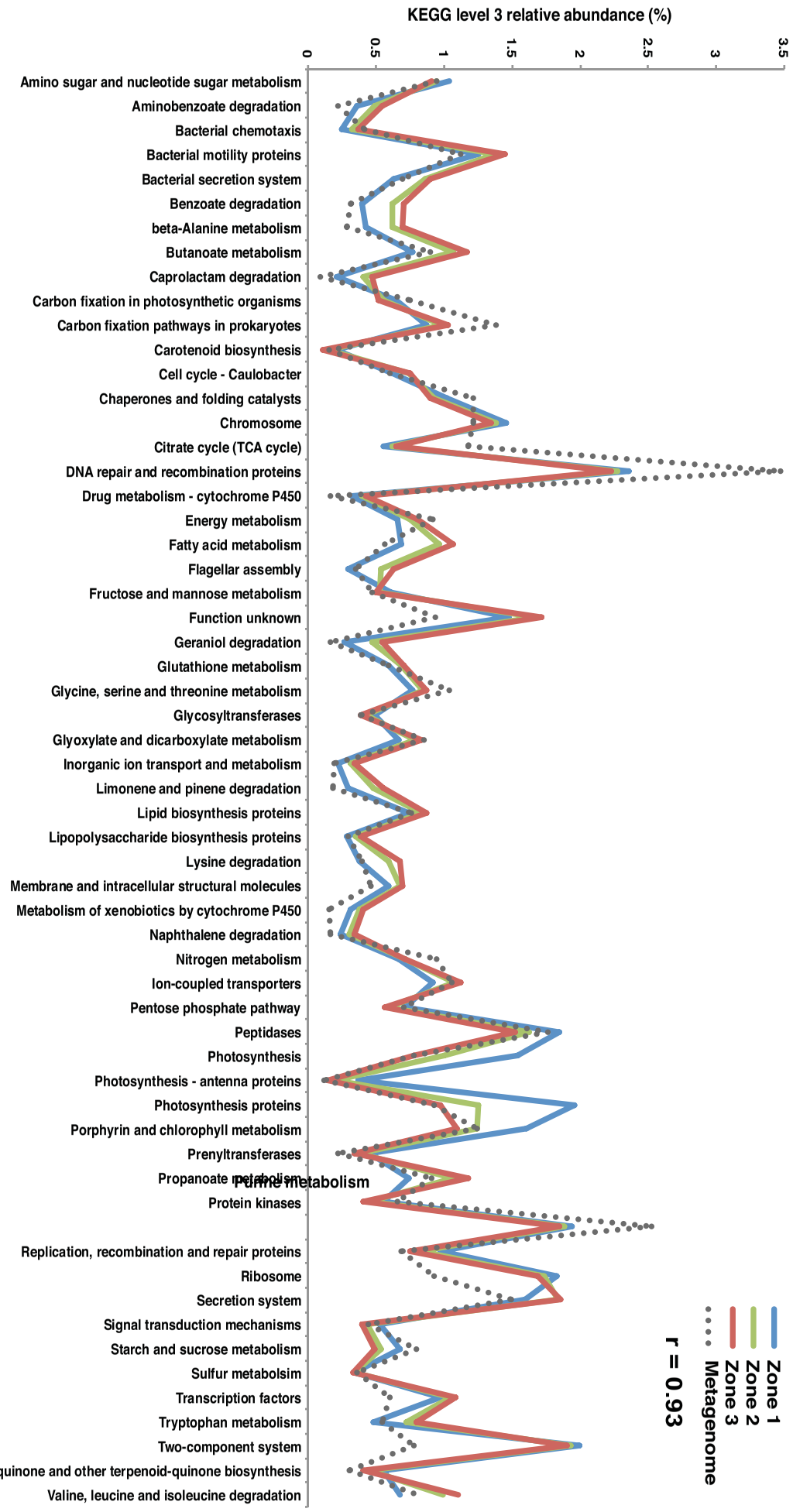
KEGG level 3 relative abundance (%)
0
0.5
1
1.5
2
2.5
3
3.5
Amino sugar and nucleotide sugar metabolism
Aminobenzoate degradation
Bacterial chemotaxis
Bacterial motility proteins
Bacterial secretion system
Benzoate degradation
beta-Alanine metabolism
Butanoate metabolism
Caprolactam degradation
Carbon fixation in photosynthetic organisms
Carbon fixation pathways in prokaryotes
Carotenoid biosynthesis
Cell cycle - Caulobacter
Chaperones and folding catalysts
Chromosome
Citrate cycle (TCA cycle)
DNA repair and recombination proteins
Drug metabolism - cytochrome P450
Energy metabolism
Fatty acid metabolism
Flagellar assembly
Fructose and mannose metabolism
Function unknown
Geraniol degradation
Glutathione metabolism
Glycine, serine and threonine metabolism
Glycosyltransferases
Glyoxylate and dicarboxylate metabolism
Inorganic ion transport and metabolism
Limonene and pinene degradation
Lipid biosynthesis proteins
Lipopolysaccharide biosynthesis proteins
Lysine degradation
Membrane and intracellular structural molecules
Metabolism of xenobiotics by cytochrome P450
Naphthalene degradation
Nitrogen metabolism
Ion-coupled transporters
Pentose phosphate pathway
Peptidases
Photosynthesis
Photosynthesis - antenna proteins
Photosynthesis proteins
Porphyrin and chlorophyll metabolism
Prenyltransferases
Propanoate metabolism
Purine metabolism
Protein kinases
Replication, recombination and repair proteins
Ribosome
Secretion system
Signal transduction mechanisms
Starch and sucrose metabolism
Sulfur metabolsim
Transcription factors
Tryptophan metabolism
Two-component system
Ubiquinone and other terpenoid-quinone biosynthesis
Valine, leucine and isoleucine degradation
Zone 1
Zone 2
Zone 3
Metagenome
r = 0.93

A

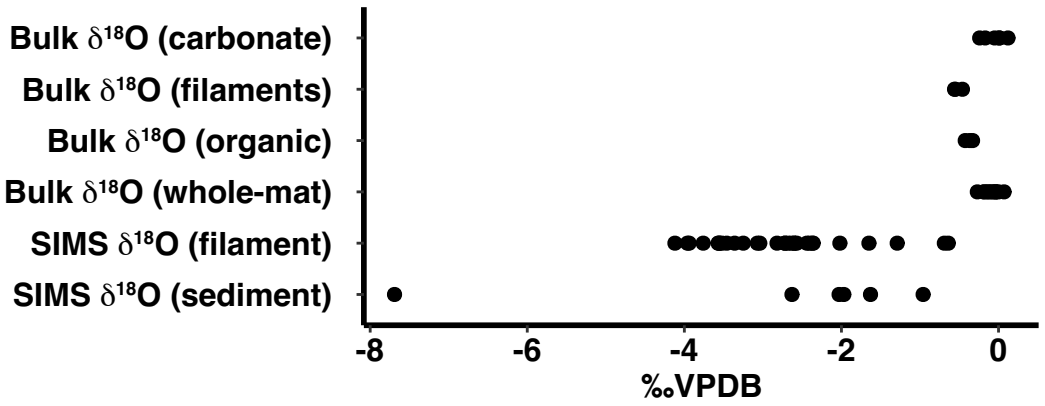
Bulk δ18O (carbonate)
Bulk δ18O (filaments)
Bulk δ18O (organic)
Bulk δ18O (whole-mat)
SIMS δ18O (filament)
SIMS δ18O (sediment)
-8
-6
-4
-2
0
‰VPDB

B

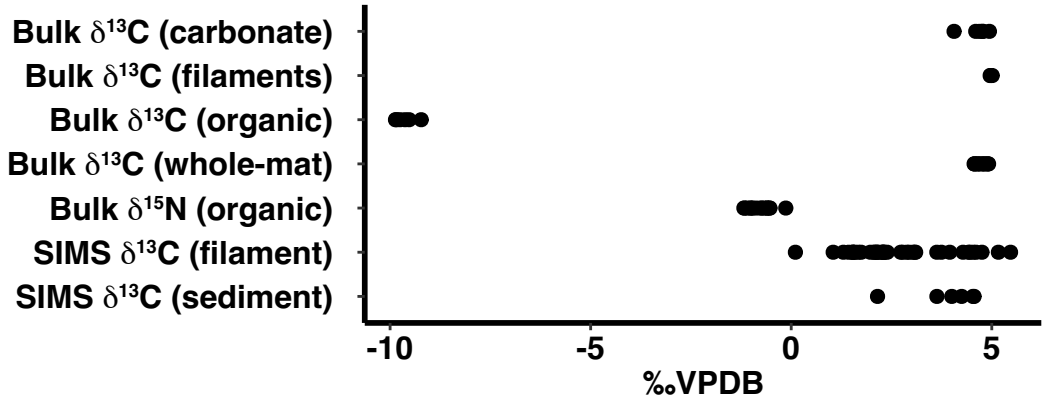
Bulk δ13C (carbonate)
Bulk δ13C (filaments)
Bulk δ13C (organic)
Bulk δ13C (whole-mat)
Bulk δ15N (organic)
SIMS δ13C (filament)
SIMS δ13C (sediment)
-10
-5
0
5
‰VPDB

C

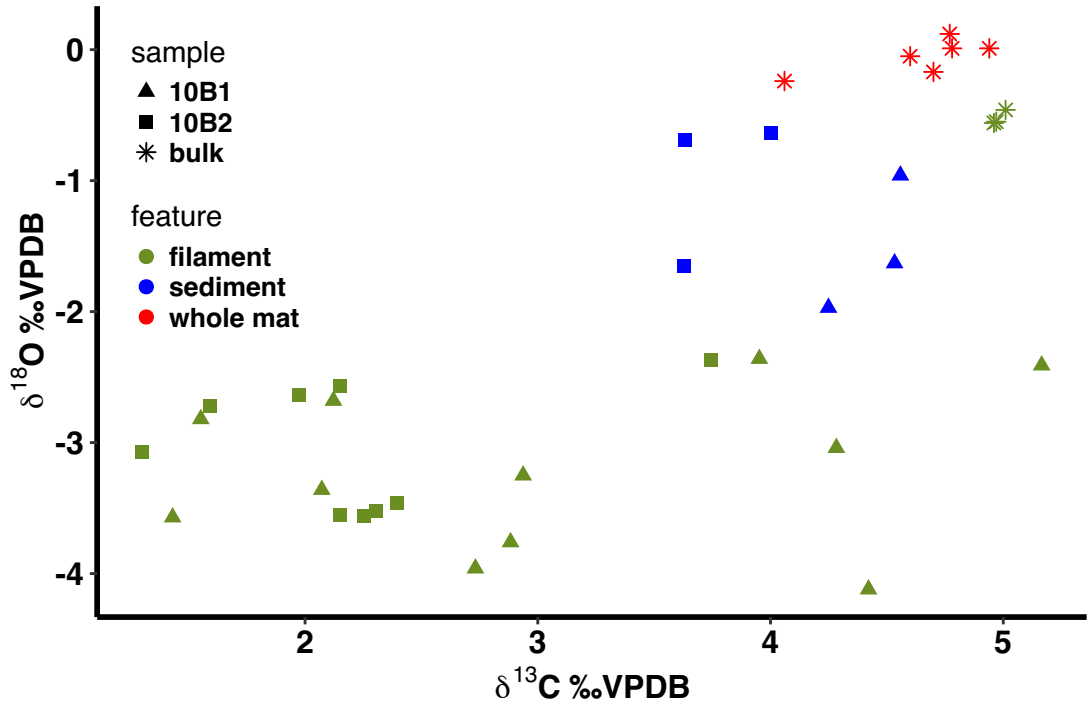
sample
10B1
10B2
bulk
feature
filament
sediment
whole mat
0
-1
-2
-3
-4
δ18O ‰VPDB
2
3
4
5
δ13C ‰VPDB

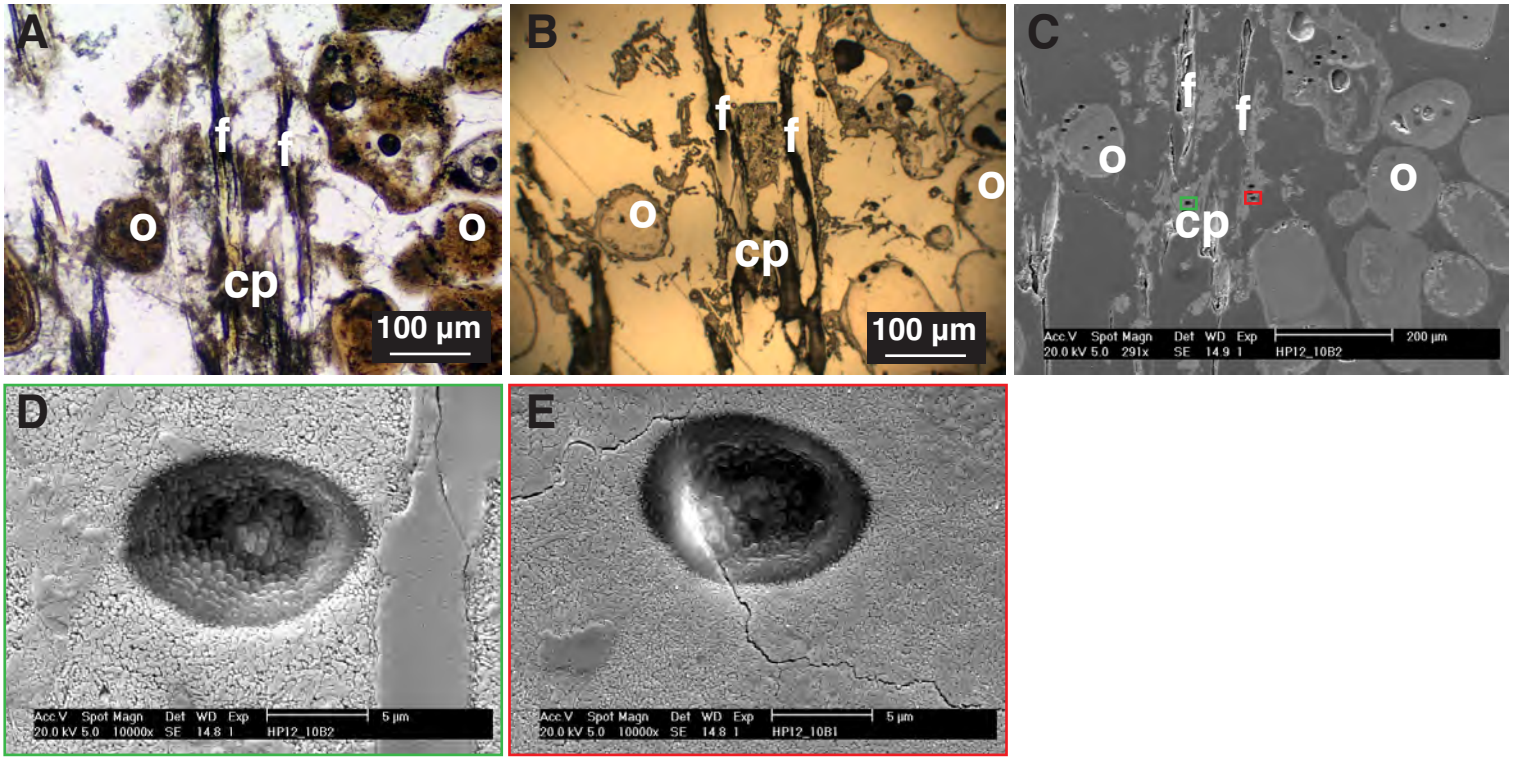
A
f
f
o
o
cp
100 µm
B
f
f
o
o
cp
100 µm
C
f
f
o
o
cp
Acc.V Spot Magn Det WD Exp
20.0 kV 5.0 291x SE 14.9 1 HP12_10B2
200 µm
D
Acc.V Spot Magn Det WD Exp
20.0 kV 5.0 10000x SE 14.8 1 HP12_10B2
5 µm
E
Acc.V Spot Magn Det WD Exp
20.0 kV 5.0 10000x SE 14.8 1 HP12_10B1
5 µm

TABLE 1. SUMMARY STATISTICS FOR THROMBOLITE SAMPLES BY ZONE FOR BACTERIA AND ARCHAEA SAMPLES

	Bacteria			*Archaea*		
	Zone 1	*Zone 2*	*Zone 3*	*Zone 1*	*Zone 2*	*Zone 3*
Depth	0-3 mm	3-5 mm	5-9 mm	0-3 mm	3-5 mm	5-9 mm
No. of Reads	25609	21535	31217	14253	22794	21646
Normalized Reads[a]	3691	3691	3691	3587	3587	3587
Total OTUs[b]	2044	2947	3525	671	506	654
OTUs >0.005%	729	949	956	178	169	172
Shannon Index[c]	6.59	8.67	8.59	4.91	3.58	3.97
±sd	±0.026	±0.026	±0.016	±0.008	±0.020	±0.024
(confidence)	(0.029)	(0.029)	(0.019)	(0.009)	(0.023)	(0.027)
% coverage[d]	94.5	87.8	92.3	97.9	98.2	98.2
±sd	0.13	5.02	0.71	0.07	0.09	0.31

[a]Randomized sequence count of each replicate for each zone used to measure diversity.
[b]OTU identification used a 97% similarity threshold.
[c]Shannon diversity index calculated over ten iterations for three replicate samples.
[d]Goods coverage estimate.

Supplemental Figure S1

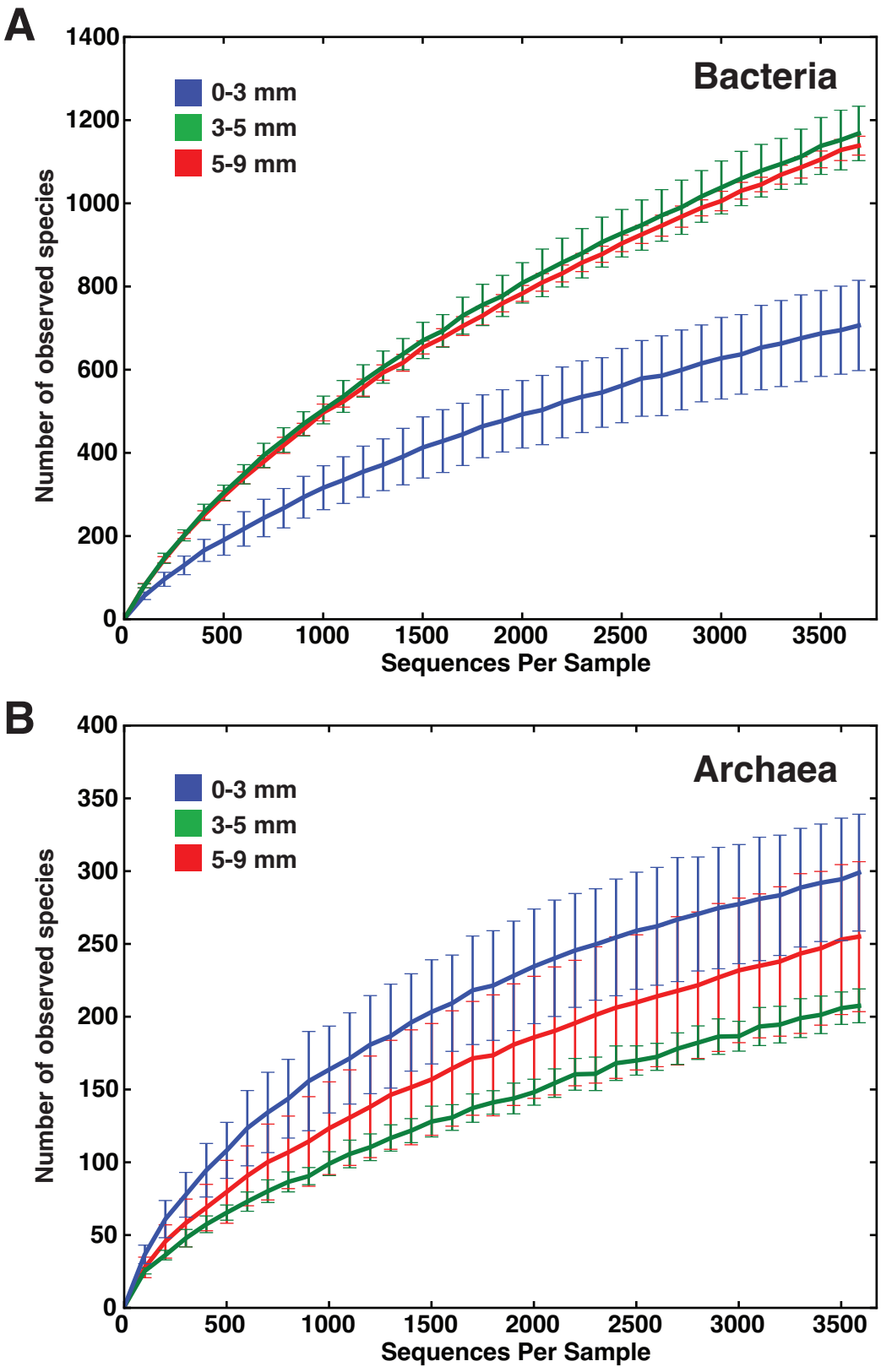

Supplemental Figure S2

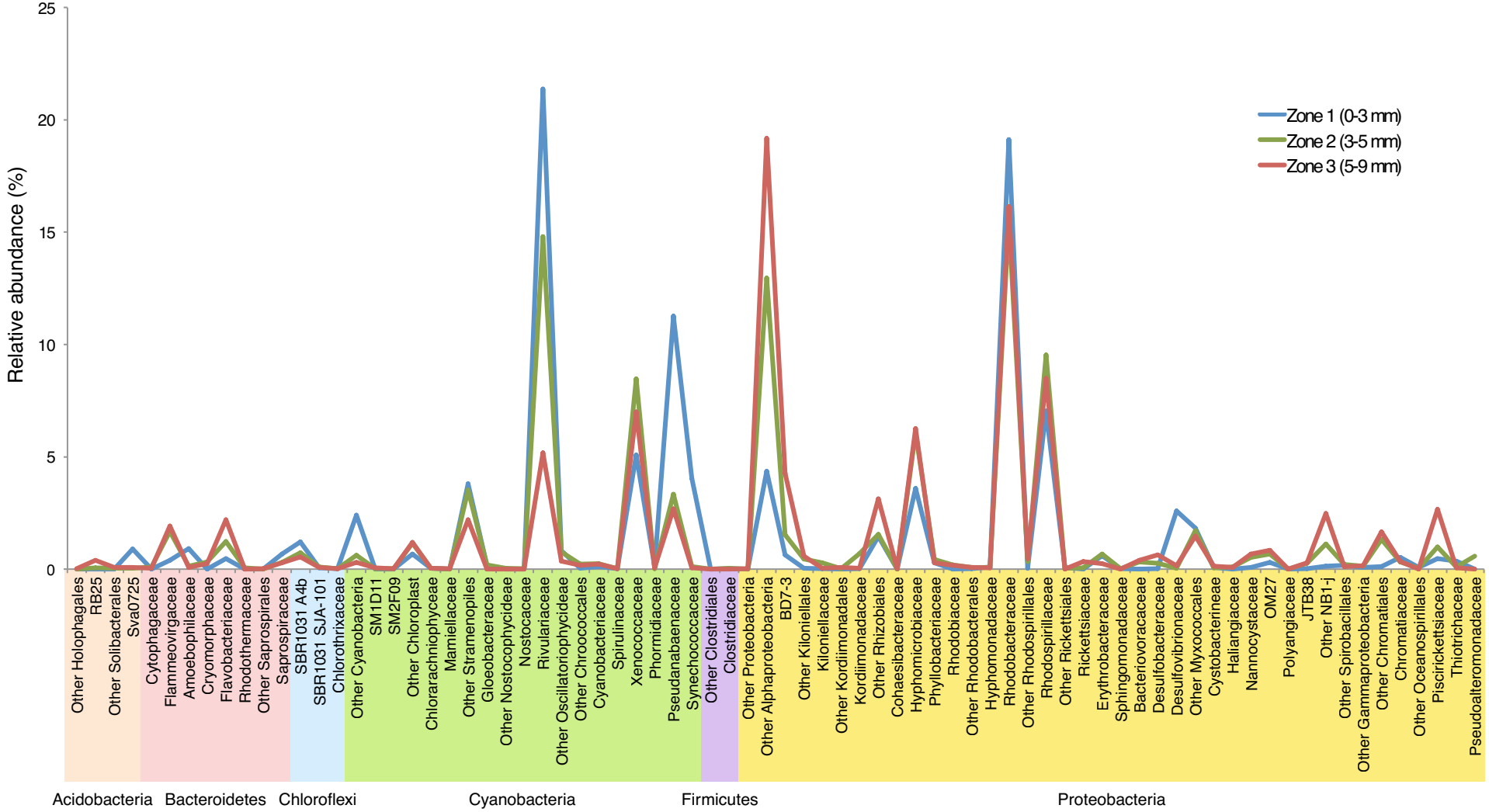

Supplemental Figure S3

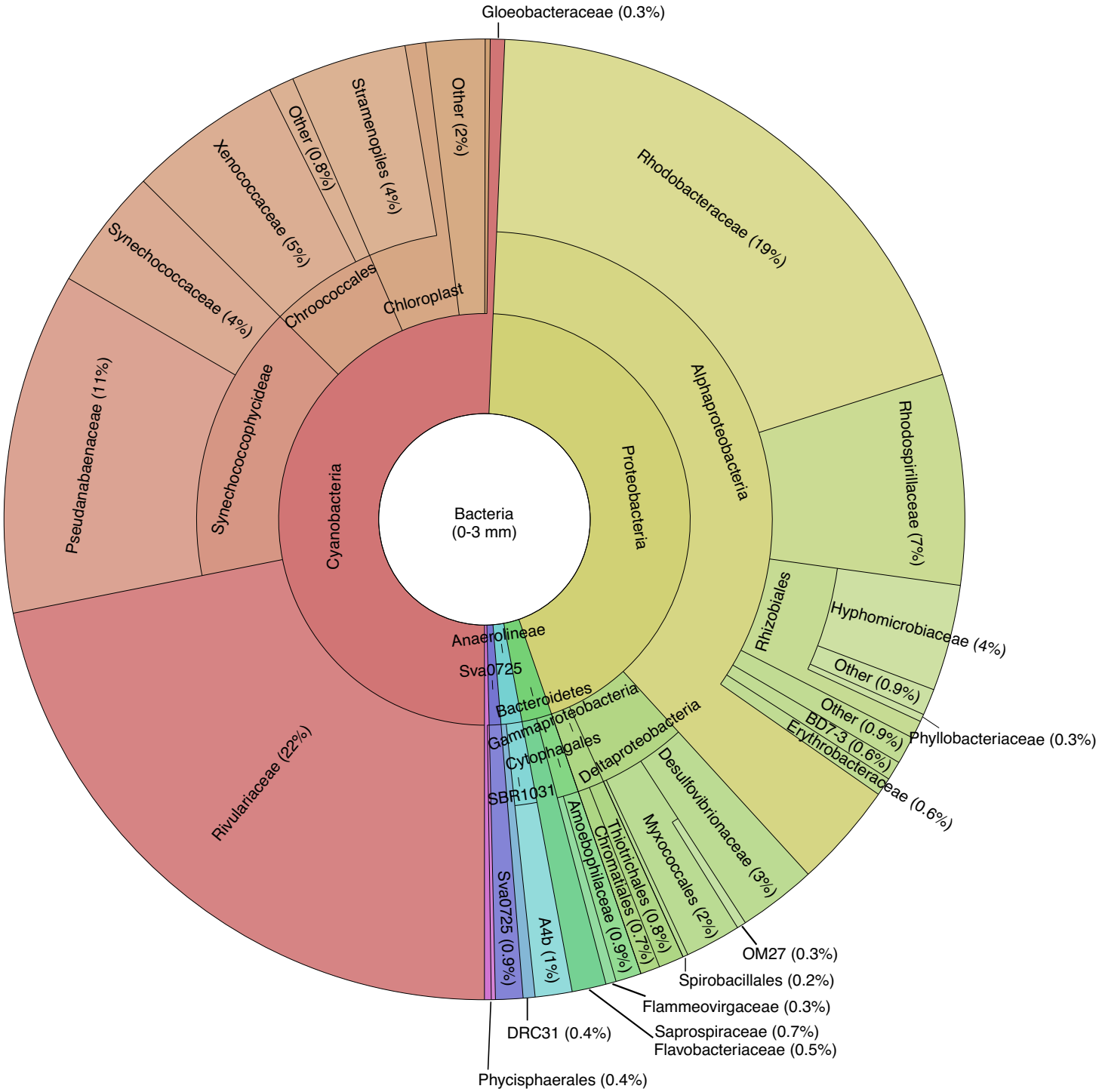

Supplemental Figure S4

Supplemental Figure S5

SUPPLEMENTARY TABLE S1. PRIMER LIST USED TO GENERATE TITANIUM 454 BARCODED LIBRARIES FOR BACTERIA AND ARCHAEA

Specificity	*Primer ID*	*Sample*	*454 Primer*[a]	*Barcode*[b]	*Linker*	*16S Primer*	*16S rRNA primer reference*[c]
bacteria	Bac27F-T	Bacteria	A	none	TC	AGAGTTTGATCCTGGCTCAG	Suzuki & Giovannoni, 1996
universal	Bac338R-01-T	Zone 1	B	CCAACCTT	CA	TGCTGCCTCCCGTAGGAGT	Suzuki & Giovannoni, 1996
universal	Bac338R-02-T	Zone 1	B	GGAATTGG	CA	TGCTGCCTCCCGTAGGAGT	Suzuki & Giovannoni, 1996
universal	Bac338R-03-T	Zone 1	B	AACCAACC	CA	TGCTGCCTCCCGTAGGAGT	Suzuki & Giovannoni, 1996
universal	Bac338R-04-T	Zone 2	B	TTAAGGCC	CA	TGCTGCCTCCCGTAGGAGT	Suzuki & Giovannoni, 1996
universal	Bac338R-05-T	Zone 2	B	CCGGCCTT	CA	TGCTGCCTCCCGTAGGAGT	Suzuki & Giovannoni, 1996
universal	Bac338R-06-T	Zone 2	B	AAGGCCTT	CA	TGCTGCCTCCCGTAGGAGT	Suzuki & Giovannoni, 1996
universal	Bac338R-07-T	Zone 3	B	AACGAAGC	CA	TGCTGCCTCCCGTAGGAGT	Suzuki & Giovannoni, 1996
universal	Bac338R-08-T	Zone 3	B	TTCGAAGC	CA	TGCTGCCTCCCGTAGGAGT	Suzuki & Giovannoni, 1996
universal	Bac338R-09-T	Zone 3	B	AATACCGC	CA	TGCTGCCTCCCGTAGGAGT	Suzuki & Giovannoni, 1996
archaea	Arc23F[e]	Archaea	none	none	none	ATTCCGGTTGATCCTGC	Barns et al., 1994
archaea	Arc958R[d,e]	Archaea	none	none	none	YCCGGCGTTGAMTCCATTT	Delong, 1992
archaea	Arc344F-T[d]	Archaea	A	none	TC	ACGGGGYGCAGCAGGCGCGA	Casamayor et al., 2002
archaea	Arc915R-01-T	Zone 1	B	CCAACCAA	CA	GTGCTCCCCCGCCAATTCCT	Casamayor et al., 2002
archaea	Arc915R-02-T	Zone 1	B	CGAACCAT	CA	GTGCTCCCCCGCCAATTCCT	Casamayor et al., 2002
archaea	Arc915R-03-T	Zone 1	B	AGACAGTG	CA	GTGCTCCCCCGCCAATTCCT	Casamayor et al., 2002
archaea	Arc915R-04-T	Zone 2	B	AGACACAG	CA	GTGCTCCCCCGCCAATTCCT	Casamayor et al., 2002
archaea	Arc915R-05-T	Zone 2	B	CCAACGTA	CA	GTGCTCCCCCGCCAATTCCT	Casamayor et al., 2002
archaea	Arc915R-06-T	Zone 2	B	CATCTCGT	CA	GTGCTCCCCCGCCAATTCCT	Casamayor et al., 2002
archaea	Arc915R-07-T	Zone 3	B	CATCTCCA	CA	GTGCTCCCCCGCCAATTCCT	Casamayor et al., 2002
archaea	Arc915R-08-T	Zone 3	B	CAGTGTGT	CA	GTGCTCCCCCGCCAATTCCT	Casamayor et al., 2002
archaea	Arc915R-09-T	Zone 3	B	CCGGATTA	CA	GTGCTCCCCCGCCAATTCCT	Casamayor et al., 2002

a. 454 Life Sciences sequence primers A (CTATGCGCCTTGCCAGCCCGCTCAG) and B (CGTATCGCCTCCCTCGCGCCATCAG) with a TC or CA linker, respectively, preceding the 16S primer sequence.
b. Barcodes sequences from Hamady *et al*., 2008.
c. References are for 16S rRNA gene primer.
d. Primers contain degenerate bases: Y (C,T), M (A,C).
e. *Archaea* specific 16S rRNA gene primers used for initial amplification of a nested PCR.

SUPPLEMENTAL TABLE S3. PERCENT OF KEY ELEMENTS BY WEIGHT FOUND IN THE THROMBOLITE-FORMING MICROBIAL MAT

	n	*%C (s.e.)*	*%N (s.e.)*	*%CaCO3 (s.e.)*
Whole mat	12	12.05 (0.037)	0.17 (0.003)	91.72 (0.24)
Organic	6	43.1 (0.598)	3.26 (0.168)	-
Inorganic	6	-	-	93.33 (0.649)
Filament	1	-	-	45.87 (n/a)